Simultaneous reduction of carbon dioxide and energy harvesting using RGO-based SiO$_2$-TiO$_2$ nanocomposite for supercapacitor and microbial electrosynthesis

Abdul Hakeem Anwer [a,1], Mohd Shoeb [a,*,1], Fouzia Mashkoor [a], Aleesha Ali [b], Sumairah Kareem [c], Mohd Zahid Ansari [d], Jang Min Park [a], Changyoon Jeong [a,*]

[a] School of Mechanical Engineering, Yeungnam University, Gyeongsan 38541, Republic of Korea
[b] Chemical Engineering Research Center, School of Chemical Engineering and Technology, Tianjin University, Tianjin, China
[c] Interdisciplinary Nanotechnology Centre (INC), ZHCET College, Aligarh Muslim University, Aligarh 202002, India
[d] School of Materials Science and Engineering, Yeungnam University, Gyeongsan 38541, Republic of Korea

ARTICLE INFO

ABSTRACT

Nowadays, developing a simple, economical, and scalable approach for producing energy storage and harvesting devices remains challenging. Herein, we developed a mesoporous RGO-SiO$_2$-TiO$_2$ nanocomposite for the electroreduction of carbon dioxide through microbial electrosynthesis and high-performance supercapacitor device. An electrode containing Si/Ti oxide nanoparticles and a layer of RGO coated on carbon felt containing RGO-SiO$_2$-TiO$_2$ NCs demonstrated stable photocurrents 2.1 times higher than a bare carbon felt electrode and acetate production of 3.21 mM/d with a coulombic Efficiency of acetate 78% and a current density 2.7 A/m^2, which was metabolized into acetate from HCO$_3$ by cultivated anaerobic bacteria. The RGO-SiO$_2$-TiO$_2$ NCs-based supercapacitor achieved a maximum energy density of 35 Wh/kg at 630 W/kg power density, and after 10,000 cycles, it retained 84% capacitance stability at 10 A/g with 180 F/g at 1.25 A/g. This method presents a straightforward, cost-effective approach for mitigating CO$_2$ emissions and generating energy harvesting devices.

1. Introduction

Fossil fuels, pivotal in meeting global energy demands, are progressively depleting, and their extensive utilization in contemporary society has significantly contributed to the occurrence of global warming via the emission of carbon dioxide (CO$_2$) into the atmosphere [1,2]. In recent years, the diminishing availability of fossil fuels has fueled an escalating call for alternative energy sources. Moreover, the pressing need for dependable alternatives has been amplified by the burgeoning market for portable electronic devices [3]. In response to these environmental and energy challenges, there has been a growing awareness and focus on the study of renewable and clean energy sources. Among the promising options, bio-photocatalytic CO$_2$ reduction has emerged as a viable and sustainable solution. This process offers several advantages, including low-cost, clean energy generation, and environmentally friendly characteristics. Through bio-photocatalytic reduction of CO$_2$, both carbon dioxide (CO$_2$) and inorganic carbon (HCO$_3^-$) can be

converted into valuable biofuels, such as acetic acid, ethyl alcohol, butyrate, and CH$_4$, using renewable radiation. This pioneering methodology presents a hopeful trajectory for alleviating the global environmental and energy challenges of today, while concurrently offering a sustainable reservoir of biofuels with diverse applications. In the realm of sustainable and cutting-edge methodologies, Microbial Electrosynthesis (MES) has emerged as a promising and novel approach to convert inorganic carbon sources, such as bicarbonate (HCO$_3^-$) or carbon dioxide (CO$_2$), into valuable building block chemicals. MES systems employ electrotrophs as biological catalysts, making them a potentially effective method for generating sustainable energy and reducing carbon emissions. Electrotrophs play an essential role in the reduction of carbon dioxide (CO$_2$) or bicarbonate (HCO$_3^-$) into valuable building block chemicals in MES systems. These processes involve the use of electrotrophs as electron acceptors, which can either acquire electrons indirectly by assimilating soluble electron carriers such as H$_2$ or directly through cathodic electron transfer in MES. Electrotrophs utilize

electrons to convert CO_2 into reactive acetyl-CoA, which is subsequently oxidized to acetate during ATP phosphorylation via the Wood-Ljungdahl pathway (WLP), as described by Ragsdale and Pierce in 2008 [4]. However, the interaction between electrotrophs and plain electrodes is a limiting factor in this process, leading to a decrease in the current density of CO_2 reduction. This limitation arises from the lack of effective electron transfer between the electrotrophs and the plain electrodes, which is a critical bottleneck in the overall process. As an example, in order to increase the output of chemical substances like acetate, it could prove advantageous to amplify the circuital current or current density of the MES cell, leading to a greater abundance of cathodic electrons. An instance of this concept can be seen in the electrochemical reduction of inorganic carbon (IC) to acetate (Reaction 1), which has been demonstrated with differing levels of success in MES systems utilizing both pure cultures and multispecies inoculations (mixed cultures). MES holds promise as a sustainable and innovative approach for producing valuable chemicals through the utilization of electrotrophs as electron acceptors in the microbial transformation of carbon compounds [5,6]. Typically, the immobilization of cultures takes place on a variety of cathodic electrode materials (as shown in Table S1), such as carbon-based metals (Cu, Ni, Au, Fe,), and Reduce graphene oxides [7]. The primary role of these materials is to decrease the resistance to electron transfer between the cathode electrode and the immobilized electrotrophs. This results in an increase in circuital current, which supports the electrotrophic conversion of IC to acetate (as summarized in Table S1) [8–10]. Another strategy to enhance the circuital current (current density) necessary for electrotrophic reduction of IC in MES biocathodes is through the utilization of photocatalytic semiconductor materials that are responsive to solar radiation [11–14]. The bacteria may get additional electrons and hydrogen from the exciting semiconductor under the felicitous condition, which will boost the electrotrophic via indirect (H_2 or mediators) or direct reduction of carbon (HCO_3^- or CO_2). By combining artificial and natural platforms, it is feasible to develop novel catalytic systems that may possess superior functionality compared to the individual catalytic functions taken in isolation [12]. This technique employs solar radiation to directly stimulate semiconducting substances, while simultaneously removing aqueous pollutants from the anodic chambers. This renders the approach an effective and environmentally sustainable method for both remediating the environment and producing renewable energy. The direct utilization of solar light as the energy source for exciting the semiconductors, coupled with the concomitant elimination of aqueous contaminants in the anodic chambers, offers a promising and sustainable strategy with potential applications in addressing environmental pollution and generating renewable energy [14].

$$2HCO_3^- + 4H_2 + H^+ \rightarrow CH_3COO^- + 4H_2O \qquad (1)$$
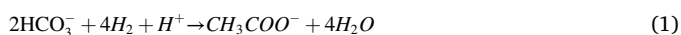
Appropriate photocatalytic materials with semiconducting properties for this application should exhibit excellent biocompatibility with the electrotrophs, optimal band gaps, and other desirable characteristics such as low overpotentials, non-toxicity and long-term stability towards the electrotrophs. The chosen materials should be compatible with the electrotrophs at a biological level, and possess favorable electronic band gaps to facilitate efficient electron transfer processes. Furthermore, these materials should exhibit low overpotentials, which are the additional energy requirements needed for the electrochemical reactions to occur, to enhance the energy efficiency of the system. The durability over extended periods and non-harmfulness towards the electrotrophic microorganisms are also essential factors to guarantee the continued effectiveness and feasibility of the photocatalytic substances in the system [14,15].

The pioneering work of Liu et al. in 2015 introduced the concept of photoelectrode-assisted MES for carbon dioxide (CO_2) reduction [16]. This innovative approach involved the use of a Si nanowire photocathode and a TiO_2 photoanode in a solar-assisted MES system. The photoelectrode in the system effectively captured solar energy and transferred reducing equivalents to *Sporomusa ovata*, a microorganism renowned for its ability to produce acetate. Moreover, the acetate was utilized as a precursor for the synthesis of longer carbon chains through recombinant *Escherichia coli* in this approach [2,17]. In subsequent research, photo-assisted biocathodes, including $WO_3/MoO_3/g$-C_3N_4 [18] and Ag_3PO_4/g-C_3N_4 [19], with Z-scheme heterojunctions, have been fabricated utilizing *Serratia marcescens* Q1 as the biocatalyst. In this approach, photo-generated electrons enhanced hydrogen production, which, in turn, promoted CO_2 fixation by the biocatalyst for acetate synthesis. In contrast to conventional MES systems that employ pure bacterial strains as biocatalysts, mixed cultures showed higher acetate production and better resistance to environmental variations, perhaps due to synergistic effects [20,21]. However, the understanding of the efficiency of MES utilizing mixed cultures as biocatalysts, in combination with the assistance of photocathodes, is currently limited and necessitates additional research. Hence, it is imperative to develop superior and more effective photocatalysts in order to optimize the conversion of CO_2 and enhance the rates of yield with enhanced selectivity.

Among the numerous photocatalysts, titanium dioxide (TiO_2) is widely recognized as a preeminent semiconductor (SC) material for photocatalytic processes, owing to its abundance, cost-effectiveness, photostability, and non-toxicity [22]. However, TiO_2 can only be activated under UV light irradiation because of its wide band gap energy (3.20 eV for anatase), which limits its efficiency for CO_2 reduction. Moreover, TiO_2 has been reported to have lower efficiency and selectivity for CO_2 reduction due to the rapid recombination of photo-generated electron-hole pairs (e^-/h^+) [23–25]. Therefore, it is crucial to alter the TiO_2 structure to hinder the electron and hole pairs' recombination rate, thereby enabling efficient CO_2 photoreduction to valuable chemicals and fuels [26,27].

To address the previously stated concerns, a common method to enhance the photoactivity of TiO_2 is by utilizing metal/metal oxide nanoparticles. These nanoparticles are incorporated into TiO_2 to increase its effectiveness in the visible spectrum and compensate for its low surface area [28–31]. The incorporation of TiO_2 into Silicon dioxide (SiO_2) porous materials can lead to an array of advantages for photocatalytic reactions. These benefits include improved molecular diffusion towards active sites and enhanced surface area. This research also highlights the drawbacks of unsupported catalysts. An alternative strategy to augment the catalytic performance involves incorporating reduced graphene nanosheets (RGO) into the photo-nanocatalysts to maximize the surface area, thus further enhancing the potential for efficient catalytic reactions [28]. Graphene is a highly promising material due to its exceptional electrical conductivity, permeability, thermal and chemical stability, as well as its substantial surface area and cost-effectiveness. It has potential as an active material for a wide range of applications, including its use as an electrode material [32]. Graphene, composed of a single layer of sp^2-bonded carbon atoms arranged in a hexagonal lattice, exhibits remarkable properties such as exceptional thermal and electrical conductivity, remarkable strength, and an extraordinarily large specific surface area (measuring 2675 m^2/g), rendering it a highly attractive choice for various applications [33]. RGO nanosheet is a versatile nanomaterial that plays a crucial role in modulating the catalytic behavior of metal oxide-graphene nanocomposites. The combination of reduce graphene and Titania can reduce the recombination of charges (i.e., e^- and h^+) and improve access to active sites, leading to increased photocatalytic activity. Moreover, ordered mesoporous silica can act as an excellent reinforcing agent due to its highly organized mesostructure, substantial surface area, controllable pore size, and thermal stability. These attributes contribute to improved microbial electrosynthesis and supercapacitor activity, particularly in the visible region, as well as increased surface area for enhanced performance.

The purpose of this research is to introduce a new method for

synthesizing an effective mesoporous nanostructure consisting of SiO_2, TiO_2 and RGO using Pluronic F-68 as a soft template, via a sol-gel co-condensation method combined with hydrothermal treatment. It has been recently discovered that certain materials can be utilized for multiple applications, making them highly attractive for developing efficient and cost-effective systems. Employing a single material for dual purposes simplifies the design and reduces the overall cost of the system, which could significantly impact the advancement of sustainable energy technologies. Our study reports on the first dual application of RGO-SiO_2-TiO_2 nanocomposites. Firstly, they serve as structured electrodes in a photo-assisted MES (Microbial Electrosynthesis) system. The RGO is deposited on carbon felt and covered with Ti/Si oxide nanoparticles. The photo-assisted MES system is hypothesized to generate long-lived electrons and holes through irradiation of the Z-scheme of RGO-SiO_2-TiO_2 heterojunctions, which are then used for proton reduction to produce H_2 and bio-assimilated to produce Ac (Reaction 1), while electrons from the anodic chamber fill the semiconductor holes. Secondly, electrochemical experiments demonstrate that RGO-SiO_2-TiO_2 nanocomposites exhibit favorable specific capacitance and stability when used as supercapacitor electrodes, and the charge storage mechanism of the electrochemical supercapacitor is evaluated using Trassati method and develop a supercapacitor device.

The incorporation of SiO_2-TiO_2 NCs into RGO acted as a conductive additive and improved charge transportation, electrode-electrolyte accessibility, and electrochemical reaction kinetics. The highly porous RGO-SiO_2-TiO_2 NCs with a large surface area, along with the synergistic combination of RGO, led to a significant improvement in the performance of the supercapacitor by a factor of 1.25 and the MES effectiveness by 2.1. The synthesized RGO-SiO_2-TiO_2 NCs were used to fabricate a symmetric supercapacitor device (SSD), which displayed a high specific capacitance of 180 F/g at a current density of 1.25 A/g and a high energy density of 35 Wh/kg at a power density of 630 W/kg. The SSD device also exhibited good durability, retaining 84% of specific capacitance after 10,000 charge-discharge cycles. Overall, this study demonstrated an effective synthesis approach for developing nanocomposites, which can be used as an excellent nanocomposite device for energy storage.

2. Experimental

2.1. Materials and Methods

Graphene Oxide (GO) was produced by oxidizing natural graphite powder (20 μm mesh, Sigma Aldrich) using the modified Hummers method, which was also used in our previous research [2,17,24,25,32, 33]. In this experiment, Pluronic F-68 was used as a soft template for the mesoporous structure. For ease of synthesis, we used four beaker names Beaker A (2 mL of TEOS in 20 mL of ethyl alcohol), Beaker B (5 mL:
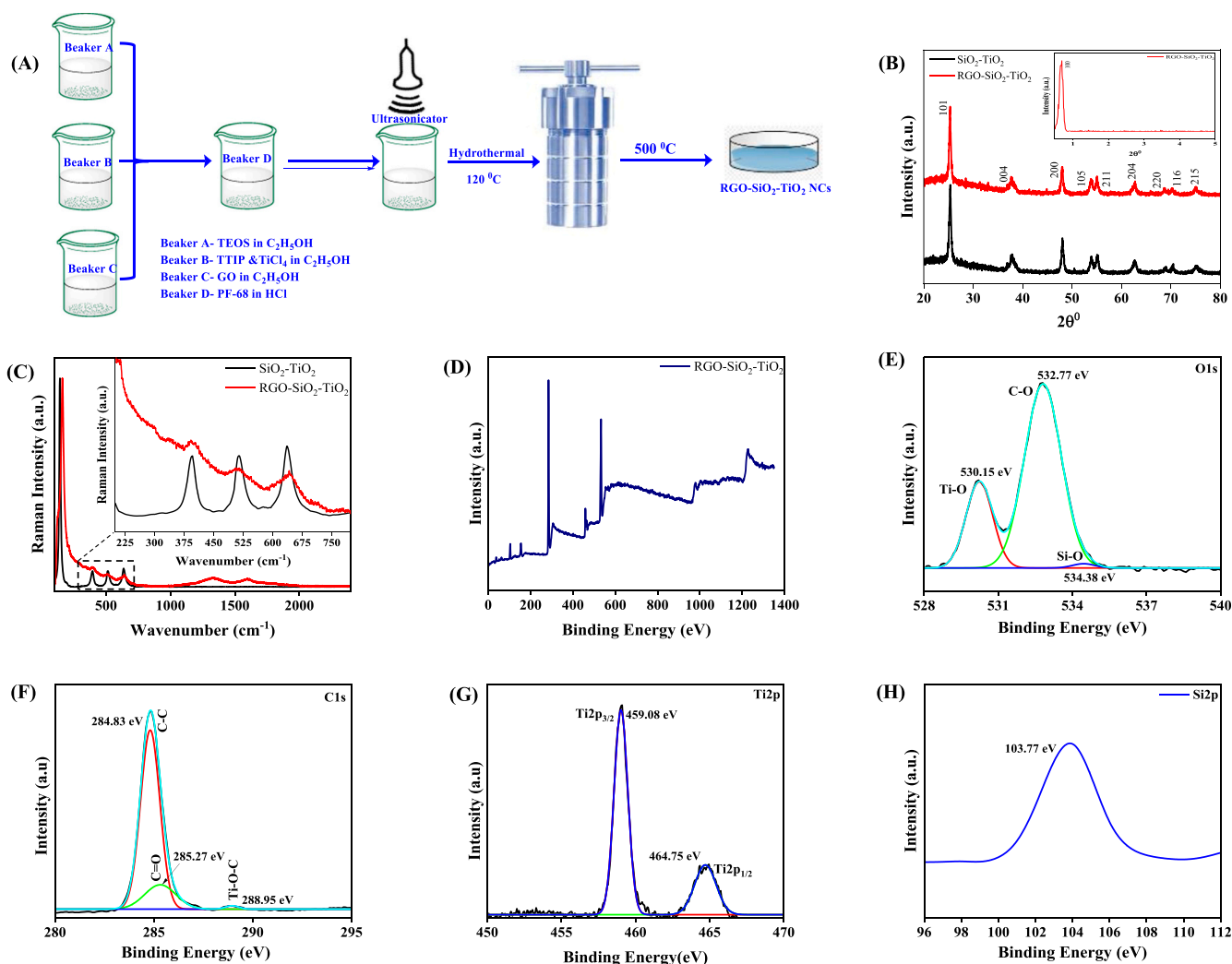

Fig. 1. Synthesis Scheme of RGO-SiO_2-TiO_2 NCs (A) XRD Pattern of SiO_2-TiO_2 NCs and RGO-SiO_2-TiO_2 NCs (inset SAXRD of RGO-SiO_2-TiO_2 NCs) (B) Raman Spectra of SiO_2-TiO_2 and RGO-SiO_2-TiO_2 NCs XPS (inset zoom between 400 and 800 cm^{-1}) (C) XPS Spectrum of RGO-SiO_2-TiO_2 NCs: Full Spectrum (D) O 1 s (E) C 1 s (F) Ti 2p (G) Si 2p (H).

1 mL TTIP: $TiCl_4$ in 20 mL of ethyl alcohol), and Beaker C (2 mg/mL of GO in 10 mL of MiliQ water). Furthermore, Beaker D contains 2 gm of Pluronic F-68 in 50 mL of 1 M HCl. Beaker A, B, and C are mixed into Beaker D, followed by the ultrasonicator (250 W) for about three hours. After the sonication, the sample was stirred for 24 h at room temperature; a semi-transparent sol was obtained. The sol was hydrothermally (Teflon-line autoclave) treated at a 2 °C/min heat rate at 120 °C for 24 h. After the preparation of the sample, it was filtered and washed with de-ionized water until the pH level became neutral. To eliminate the organic templates, the sample was then annealed in a tube furnace at 500 °C for a duration of five hours with a heating rate of 1 °C per minute (Fig. 1A). To synthesize SiO_2-TiO_2 NCs, the reaction proceeded without the GO. RGO-SiO_2-TiO_2 NCs and SiO_2-TiO_2 NCs were labeled on the samples.

2.2. SiO_2-TiO_2 and RGO-SiO_2-TiO_2 Electrodes Preparation

The RGO-SiO_2-TiO_2 as catalytic component and Nafion solution as a binder were mixed in different weight ratios and isopropanol as a solvent. Next, the mixture was subjected to ultrasonication for 60 min to disperse the components. A suspension consisting of 100.0 μL of RGO-SiO_2-TiO_2 / SiO_2-TiO_2 and Nafion paste was then extracted and coated onto a glassy carbon (GC) disk surface (diameter of 5.0 mm) using a micro-syringe, while the remainder of the suspension was reserved for coating onto a carbon felt electrode (2×1 cm^2). A muffle furnace was used to calcine the cathode after material deposition at 300 °C for 2 h. Ultrapure water was used for all aqueous solutions.

2.3. MES setup and operation

Throughout the tests used a dual-chamber photo-assisted reactor (2.5 cm diameter, 100 mL volume) with two cubic polymethyl methacrylate cylinders. Each anodic and cathodic chamber had an effective operating volume of 100 mL. The cathode was made of RGO-SiO_2-TiO_2 carbon felt, while the anode was a bare carbon felt measuring 2 cm in width and 3.5 cm in length. A cation exchange membrane (Nafion-117) was used to separate the two chambers of a reactor. All glassware and electrodes were sterilized with an autoclave before each experiment started by UV irradiation. The entire procedure was carried out on a sterile bench to minimize contamination in the MES. A non-photosynthetic electrotrophic mixed microbe was cultured in the sterile medium for 72 h and harvested after it had metabolized anaerobically IC to acetate (Ac) [7,34]. Photo-assisted MES biocathode operated without oxygen during the cultivation period and during the Ac production process, which prevented the formation of harmful reactive oxygen constituent [8] and reduced the efficiency of Ac production. Inoculating the cathodic chamber was done by resuspending cell pellets at an OD_{600} of 0.10, 0.30, 0.60, or 0.90. $NaHCO_3$ (24 mM), KH_2PO_4 (0.09 mM), NH_4Cl (2.1 mM), minerals (0.6 mL/L) and vitamins (0.6 mL/L) were the main constituents in catholyte. Prior to inoculation in the cathodic chamber, the catholyte was placed in an anaerobic glove box for 15 min, where it was sparged with N_2 gas to eliminate residual oxygen. In order to evaluate the impact of starting pH on system performance, catholyte pH was altered to 5.0 or 5.8 with 10% HCl added [35,36]. To investigate the effect of the conductivity of the solution on the system performance, the solution conductivity was adjusted to 10.3 mS/cm by adding 0.6 M KCl to the solution [6,35]. As an anolyte, phosphate buffer was used in the anodic chamber. Using this buffer anolyte prevented a significant pH shift due to hydrolysis, which would adversely affect cathode efficiency. In addition, experiments were conducted at 24 mM concentration of IC, − 1.0 V vs. Ag/AgCl of a Cathodic Potential, 10.3 mS/cm of a solution conductivities and 5.8 of pH according to Cai, et al. (2020), which conform these optimized operational parameters for Photo-assisted MES [18]. During the experiment, fed-batch reactors were operated with iodine tungsten lamps (100 W) emitting a light photon flux (virtual sunlight) [37,38]. RGO-SiO_2-TiO_2

/Carbon felt was chosen with such photon flux to maximize its activity without negatively impacting electrotrophic activity. To ensure the consistency of system performance, the fed batch process was repeated 3 times, with data being recorded after the 1st operation cycle of the reactor to ensure consistency, according to Logan's recommendation [39]. Each operating cycle was 12 h long unless otherwise noted, and then samples were taken for analysis. There were four different reactor configurations used in the control experiments. In the first reactor, the RGO-SiO_2-TiO_2/Carbon felt cathode was operated as an abiotic control without electrotrophic inoculation in order to investigate the effect of the electrotrophs on conversion of IC to Ac and synthesis of hydrogen from photogenerated electrons. The second control experiment (without light) was conducted in complete darkness to represent that lighting affects system performance accurately. In the third reactor, open-circuit conditions (OCCs) were used to determine whether electrochemical reactions assisted Ac production. As a final rector, bare carbon felt, RGO/Carbon felt, SiO_2-TiO_2/Carbon felt, or RGO-SiO_2-TiO_2/carbon felt cathodes were applied under irradiation conditions to confirm their catalytic roles.

2.4. Characterizations and electrochemical measurements

To examine the photocatalytic properties of the cathode, measurements of photocurrent response were carried out in 0.1 M Na_2SO_4 with an illumination of 26.9 kLux (light intensity) [37,38]. A cyclic voltammetry (CV) and electrochemical impedance spectrometer (EIS) analysis was performed to assess the electrochemical performance of photo-assisted biocathodes of MESs or working electrode as a supercapacitor. The CVs were performed with a potentiostat (PGSTAT204N, Metrohm Autolab, Netherlands) using a low scanning rate of 0.1 mV/s vs. Ag/AgCl and EIS with an amplitude of 5 mV was recorded between 100 kHz and 0.01 Hz. A three-electrode system was employed for CV and EIS, with the cathode electrode acting as the working electrode, the Ag/AgCl electrode used as a reference electrode, and a plain carbon felt electrode used as a counter electrode [11]. For obtaining the equivalent circuit and resistance values, Zsimpwin software was used.

2.5. Analysis and calculations

In accordance with the previous description, gas chromatography (NUCON 5700) was used to determine the concentration of Ac (mM) or the rate of production (mM/d) [11]. In the hydrogen production process, two types of hydrogen were produced: residual hydrogen (H_2) and acetate hydrogen (H_2). Based on Reaction 1, the acetate-Hydrogen was calculated as the H_2 used by the cultivated anerobic microbes to synthesize Ac [6]. Gas chromatography (NUCON 5765) was used to determine the residual hydrogen in the cathodic chamber's headspace, normalized to the catholyte volume and the operating time (m^3/m^3/d). Based on the national standard method (DZ/T 0064.49–93), the concentration of IC in catholyte was determined, and the amount of IC consumed was estimated as earlier reported [39]. To examine whether hydroxyl radicals could be generated during irradiation, by taking a sample of 1 mL of cathodic chamber electrolyte from each abiotic (without microbes) as a control was combined with benzoic acid, which scavenges the remaining amounts of OH ions to form a p-hydroxybenzoic acid [40]. The p-hydroxybenzoic acid concentration was measured by HPLC (Agilent, 1260) equipped with a UV detector according to earlier reported [40,41]. Scavenger of hole as KI was added at a concentration of 10 mM in a catholyte to determine how photogenerated holes affect the semiconductor valence-band (VB). Photo-generated holes were sufficiently scavenged with this amount, while negligible effects were felt on the solution conductivity [42,43]. The amount of biomass produced in the catholyte and cathode electrode was quantified to determine the growth of the electrotrophs in cathodic chamber. In the first step, the electrode was absorbed in a 2 mL solution of 0.2 M NaOH at 4 °C for 1 h, followed by a vortex mixer for 10 s every

15 min. In the next step, the solution was mixed with 2 mL of 0.9% salt solution (saline) and stored in a refrigerator at around − 18 °C for 1 h. After 10 min, the saline was dissolved in a water bath at about 90 °C.

The above process was repeated 3 times to determine the volume of proteins in the solution. Protein levels in the cathode effluent were measured after and before filtering through a Millipore cellulose-membrane (0.22 μm) to quantify the planktonic biomass. The overall quantity of proteins found corresponded to 80% of the bacteria's dry mass. According to Eqs. 2 and 3, coulombic efficiencies for acetate production ($CE_{acetate}$) and residual hydrogen gas production (CE_{H2}) were calculated.

$$CE_{acetate} = \frac{8 \times n_a \times F}{\int_0^t I \; dt} \times 100\% \tag{2}$$

$$CE_{H2} = \frac{2 \times n_b \times F}{\int_0^t I \; dt} \times 100\% \tag{3}$$

Where the volume of Ac is n_a (mole), the volume of hydrogen is n_b (mole), the current is I (A), the Faraday constant is F (96485 C/mole electrons), and the operation duration is t.

Using data from cyclic voltammetry (CV) and galvanostatic charge-discharge (GCD) curves, the following equations ((4) and (5)) were used to calculate the specific capacitance (C_{sp}), energy density (E_d) and power density (P_d) of the electrode material [44–46].

$$C_{sp} = \frac{\int I \; dv}{m\nu\Delta V} \tag{4}$$

$$C_{sp} = \frac{I \quad \Delta t}{\Delta V \times m} \tag{5}$$

$$E_d = \frac{I \int v(t)dt}{a \times 3.6} \tag{6}$$

$$P_d = \frac{E_d}{\triangle t} \times 3600 \tag{7}$$

Where I(A) represents the current from the CV curve, ΔV is the voltage window, ν is the scan rate or the rate of voltage change over time (in mV/s), Δt is the duration of one complete cycle, "a" is the active surface area of the device in square centimeters, and m is the mass of the sample deposited on the electrode's surface.

3. Result and Discussion

3.1. Characterization of synthesized nanocomposite

The XRD patterns of RGO-SiO₂-TiO₂ NCs and SiO₂-TiO₂ NCs are shown in Fig. 1B. The anatase phase of TiO₂ is responsible for the (101) reflection plane. XRD confirmed the anatase phase of TiO₂ NPs in samples with tetragonal structure and space group I41/amd and diffraction patterns of 25.26°, 37.67°, 48.19°, 54.15°, 54.28°, 62.51°, 69.68°, 69.75°, and 75.18°, which are equivalent to the (101), (004), (200), (105), (211), (204) (116) (220) and (215) facets (JCPDS No. 21–1272) [47]. Furthermore, no rutile phase can be seen owing to the lack of reflection at 27.4° with (110) Miller indices. The incorporation of RGO into the polymorphism of the anatase phase of TiO₂ has been found to have no effect on the crystal structure of the TiO₂ nanoparticles, which is clearly evident in the sample. The characteristic peak of RGO at 26° (002) is difficult to distinguish from the dominant peak of anatase TiO₂ NPs due to its relatively weak intensity. The XRD measurements of SiO₂-TiO₂ and RGO-SiO₂-TiO₂ confirmed the lack of contaminants. Based on the Debye-Scherer formula, we calculated crystallite sizes (D) as 15.48 nm for SiO₂-TiO₂ NCs and 12.78 nm for RGO-SiO₂-TiO₂ NCs. It was shown that RGO reduced the size of anatase SiO₂-TiO₂ NCs crystallites in the nanocomposite. Small-angle X-ray scattering (SAXS)

patterns for RGO on SiO₂-TiO₂ NCs are shown in inset Fig. 1B(inset). According to the sample alignment, the SAXS pattern's peak intensity corresponds to (100) reflection.

We performed Raman spectroscopy on the RGO-SiO₂-TiO₂ NCs and SiO₂-TiO₂ NCs to provide a clear indication of the presence of SiO₂-TiO₂ on the RGO surface (Fig. 1C). The $E_{g(1)}$, $B_{1\;g(1)}$, $A_{1\;g} + B_{1\;g(2)}$, and $E_{g(2)}$ modes of anatase TiO₂ NPs were found at 142.47, 394.89, 514.63, and 636.68 cm⁻¹ in SiO₂-TiO₂ NCs, correspondingly. Furthermore, the RGO-SiO₂-TiO₂ NCs show the mode $B_{1\;g(1)}$, $A_{1\;g} + B_{1\;g(2)}$, and $E_{g(2)}$ peaks, with a moderate blue shift (inset Fig. 1C), compared to the SiO₂-TiO₂ NCs, indicating effective SiO₂-TiO₂ NC assimilation on the RGO surface [47]. The presence of the RGO in the RGO-SiO₂-TiO₂ NCs was also verified by the 1326.03 cm⁻¹ (D band) and 1591.90 cm⁻¹ (E band) measurements (G band) [25]. The D band is a sign of optical $E_{2\;g}$ phonons of sp² carbon atoms, while the G band is a sign of defect and disorder structure, breathing mode of the sp² atoms in RGO structure. As a result, Raman spectroscopy corroborated the structural characteristics of the SiO₂-TiO₂ NCs and the interaction of the RGO on TiO₂ in the RGO-SiO₂-TiO₂ NCs, demonstrating that the structural properties of the SiO₂-TiO₂ NCs did not change as a result of the graphene connection.

The chemical composition of the RGO-SiO₂-TiO₂ NCs was determined using X-ray photoelectron spectroscopy (XPS), Fig. 1 (D, E, F, G and H). Following Gaussian fitting, the result illustrates the observed high-resolution core-level spectra of Ti 2p, Si 2p, C 1 s, and O 1 s (Full spectrum 1D). These findings demonstrated that the inorganic ingredient's electron modification disrupted Ti and O electronic surroundings. The spin-orbit doublets of Ti 2p at 459.03 eV ($2p_{3/2}$) and 464.75 eV ($2p_{1/2}$), which are related to TiO₂, are shown in the Fig. 1E. The Fig. 1F depicts the XPS spectrum of SiO₂. Si^{4+} may be assigned to Si2p at 103.85 eV. The presence of C–Si–O/Si–C–O bonds, which were formed during the interaction of SiO₂-TiO₂ with RGO, is confirmed by the deconvolution of O 1 s peaks. The Fig. 1G depicts a high-resolution spectrum of O 1 s with three distinct peaks at 530.21, 532.77, and 534.44 eV, corresponding to O atoms near oxygen vacancies Ti–O–Ti, C–O–Ti, or Si–O–Si, and C–O–Si, respectively. At the interface of TiO₂ and SiO₂, a considerable disruption of the Ti, O, and Si environment was seen; Ti-OH groups (from TiO₂) interacted with the surface Si-OH (from SiO₂) to produce the Ti-O-Si covalent bond. A Gaussian component-based fitting was applied to the C 1 s spectrum for RGO-SiO₂-TiO₂ NCs (Fig. 1H). It is attributed that the decomposed peaks are 284.84 eV, 285.30 eV, and 288.96 eV, which correspond to the binding energies of C–Si, C-Si-O, and Si–C–O bonds, and O–C═O bonds [28,47]. Furthermore, graphene's interactions with SiO₂ and TiO₂ are covalently bound as C-O-Si and C-O-Ti. The strong bonding between these chemicals throughout the supercapacitor and CO₂ reduction by microbial electrosynthesis applications ensures the nanocomposite stability.

Fig. 2 shows typical HR-TEM and SAED micrographs of mesoporous SiO₂-TiO₂ and RGO-SiO₂-TiO₂ nanocomposites. The mesoporous SiO₂-TiO₂ was depicted at 50 nm and 10 nm dimensions in Fig. 2(A and B). In Fig. 2A, TiO₂ NPs were intact onto the mesostructured SiO₂ nanoparticles with a diameter of 23 nm. Furthermore, at a scale of 10 nm, an interface between SiO₂ and TiO₂ nanoparticles can be observed in Fig. 2B, verifying the interaction at the nanoscale level. RGO-SiO₂-TiO₂ NCs are shown in Fig. 2(C, D, and E) at scales of 50 nm, 10 nm, and 2 nm. The RGO nanosheet stitched through the mesoporous SiO₂-TiO₂ NCs with the disordered interrelated nanostructure is shown in Fig. 2C. The mesoporous structure of SiO₂ with the RGO is depicted in Fig. 2D. SiO₂-TiO₂ NCs were deposited on RGO nanosheets to establish the nanostructure and see the interface of the RGO, TiO₂, and SiO₂ NPs in Fig. 2E. The nanocrystalline character of the produced sample could be seen in the HR-TEM pictures (Fig. 2E, inset) with a lattice spacing of 0.334 nm close to the lattice spacing of the anatase phase (101) plane. Furthermore, the SAED patterns Fig. 2F define the anatase phase of the RGO-SiO₂-TiO₂ NCs, with the SAED rings denoting (101), (004), (200), (105), (211), and (212) from the interior to the outside (204). The EDAX indicated the presence of graphene (as a carbon), Si, Ti, and O in Fig. 2G.
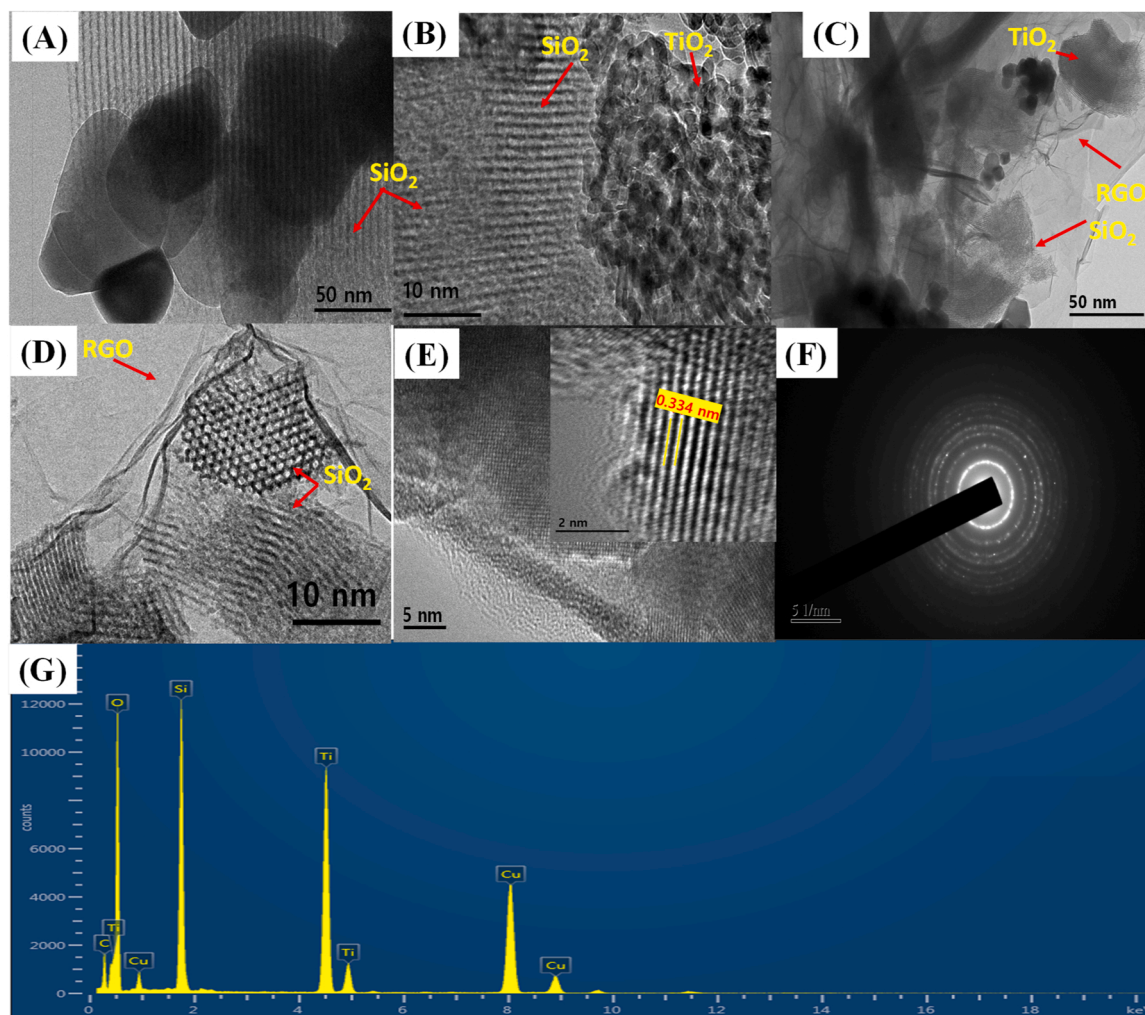
Fig. 2. HR-TEM images of SiO_2-TiO_2 (A and B at 50 nm and 10 nm scale) RGO-SiO_2-TiO_2 at 50 nm, 10 nm and 5 nm respectively (C, D and E (inset at 2 nm)) SAED Pattern (F) EDX spectra of RGO-SiO_2-TiO_2 NCs. (G).

Compared to SEM and TEM imaging techniques, the application of Brunauer–Emmett–Teller (BET) and Barrett-Joyner-Halenda (BJH) methodologies allows for the assessment of microstructural features such as specific surface area and mesoporous characteristics through analysis. The N_2 adsorption curve shown in Fig. S2 reveals distinct hysteresis loops, which conform to the H3-type hysteresis curve as described by the IUPAC for the type IV isotherm. This finding highlights the diverse nature of pore structures present in the material. The results of the analysis reveal that SiO_2-TiO_2 NCs and RGO-SiO_2-TiO_2 NCs possess a BET surface area of 275.05 m^2/g and 244.45 m^2/g, respectively (Fig. S2), and have corresponding pore sizes of 5.03 nm and 7.95 nm. These mesoporous features are critical for boosting pseudocapacitive reactions due to the availability of numerous reaction sites and the provision of easy pathways for the electrolyte ions to diffuse. The presence of well-defined mesopore sizes also enables a good contact between the dielectric solution and the material surface, thereby promoting enhanced energy storage capacity. As a result, the intricate architectures facilitated by RGO-SiO_2-TiO_2 NCs provide a more reliable substrate for achieving higher energy storage capacity.

3.2. Optimizing the electrode and MES process conditions for acetate synthesis

3.2.1. MES operational parameter adjustment for acetate synthesis

The RGO-SiO_2-TiO_2 modified electrode displayed steady and reversible photocurrent responses that were 2.29 times higher compared to electrodes made of Si/Ti oxides. This finding suggests the presence of varying degrees of electronic interaction between Si/Ti oxide species and RGO, particularly under visible light irradiation. This phenomenon indicates the significant role of RGO in enhancing the photocurrent response of the electrode and highlights the potential for synergistic effects in the composite system. Compared with biotic conditions (Fig. 3A), the abiotic controls had significantly higher photocurrents (Fig. 3B), suggesting the tradeoff between scarification, which is essential for photon capture, and electrotrophs which need to be present on electrode surfaces for the conversion of IC to Ac. Similar methods for making methane include employing indium phosphide photocathodes and *Methanosarcina barkeri* electrotrophs [12].

The Performance of RGO-SiO_2-TiO_2 photo-bioelectrochemical systems crucially calculated by the trade-off between light absorption and biocatalysis on the semiconductor-coated electrode surface. A thicker layer of electrotrophs guarantees higher bioelectrocatalytic stability and activity, while a thinner layer of electrotrophs can provide more excellent photon capture and photon transfer [12]. In subsequent experiments, the maximum Ac synthesis (Fig. S1A), the highest residual-hydrogen (Fig. S1B) and the highest photogenerated current (Fig. S1C) were achieved by changing the concentration of cultivated mixed microbes in the range (0.2–0.8) of OD_{600}. To adjust the electrode composition and loading of the composite. The RGO-SiO_2-TiO_2 loadings were increased from 0.7 to 1.40 mg/cm^2 and resulted in higher

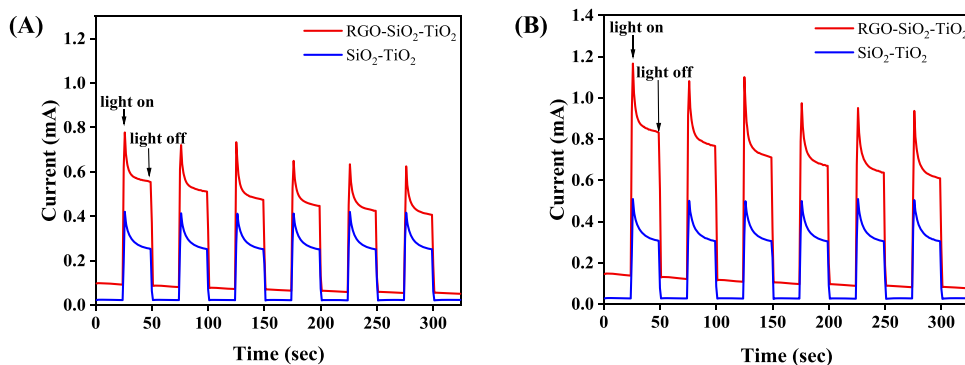**Fig. 3.** Photocurrent measurements for RGO-SiO$_2$-TiO$_2$ carbon felt, SiO$_2$-TiO$_2$ Carbon felt setup in 1.0 M Na$_2$SO$_4$ solution (A) biotic and (B) abiotic.

production of Ac (Fig. S3A), while residual hydrogen was reduced (Fig. S3B). This is attributed to the improvement in the photo-generated current (Fig. S3C). The photo-generated current was decreased with the overloading of 2.40 mg/cm^2 (Fig. S3C), resulting in reduced Ac production and greater residual-hydrogen values (Fig. S3A and B).

An appropriate ratio of RGO-SiO$_2$-TiO$_2$ of 10 (w/w, %) was achieved for the optimum RGO-SiO$_2$-TiO$_2$ loading of 1.60 mg/cm^2, resulting in the maximum production of Ac (Fig. 4A). The lowest residual-hydrogen (Fig. 4B), which corresponded the maximum photogenerated current density (Fig. 4C). As a result, the more outstanding cathodic photo-generated holes produced an additional force to push more electrons to the photo biocathode [48]. In contrast, the supplementary photoinduced current facilitated the reductive development of hydrogen, thereby enhancing the overall performance of the system. For this study, a loading of RGO-SiO$_2$-TiO$_2$ composite at 1.60 mg/cm^2, with a ratio of SiO$_2$-TiO$_2$ to RGO of 10% (w/w), was utilized for further investigations. These experimental conditions were carefully selected based on the desired composition and loading of the composite materials to ensure optimal results in subsequent analyses.

3.2.2. MES performance

Acetate was produced at a rate of 3.20 ± 0.50 mM/d via the MES with light irradiating the RGO-SiO$_2$-TiO$_2$ photocathode (Fig. 5A) with a 78 ± 5% of CE$_{acetate}$ (Fig. 5D) at a current density of 2.7 ± 0.2 A/m^2 (Fig. 5C) with an IC consumption of 22 ± 2% (Fig. S4). There were significant differences between these values and those in controls irrespective of whether they were exposed to light or not (acetate: 2.40 ± 0.05 mM/d; CE$_{acetate}$: 67 ± 5%; IC consumed: 18 ± 2% and current density: 2.2 ± 0.3 A/m^2), with SiO$_2$-TiO$_2$ or RGO separately (Fig. 5A and D; Fig. S4). This study indicates the importance of the RGO-SiO$_2$-TiO$_2$ heterojunction in the production of Ac because, similarly, the values of acetate: 1.3 ± 0.50 mM/d; CE$_{acetate}$: 50 ± 5%; IC consumed: 13 ± 3%, and current density: 1.4 ± 0.3 A/m^2 occurred irrespective of the presence of light. As shown in Fig. 5A and C, the almost complete reduce of current and Ac in the abiotic controls MES highlighted the significance of merging RGO-SiO$_2$-TiO$_2$ with cultured mixed microbes to produce Ac efficiently in photo assisted MES. In the absence of light irradiation, the RGO-SiO$_2$-TiO$_2$ MES system produced lower hydrogen production (0.1205 ± 0.005 m^3/m^3/d) than in the presence of light irradiation (0.02905 ± 0.0025 m^3/m^3/d) (Fig. 5B). This indicates that photo-generated electrons play a crucial role in hydrogen synthesis in
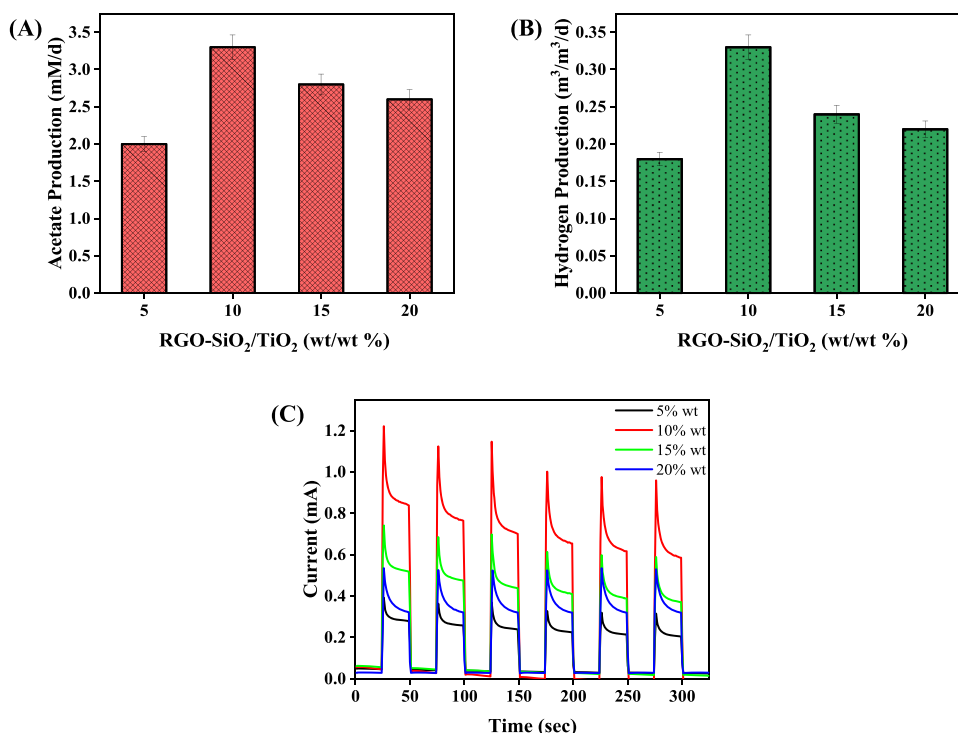

Fig. 4. (A) Effect of ratios of RGO-SiO$_2$-TiO$_2$ and RGO on production of Ac (B) Hydrogen of residual (C) photo-response curves.
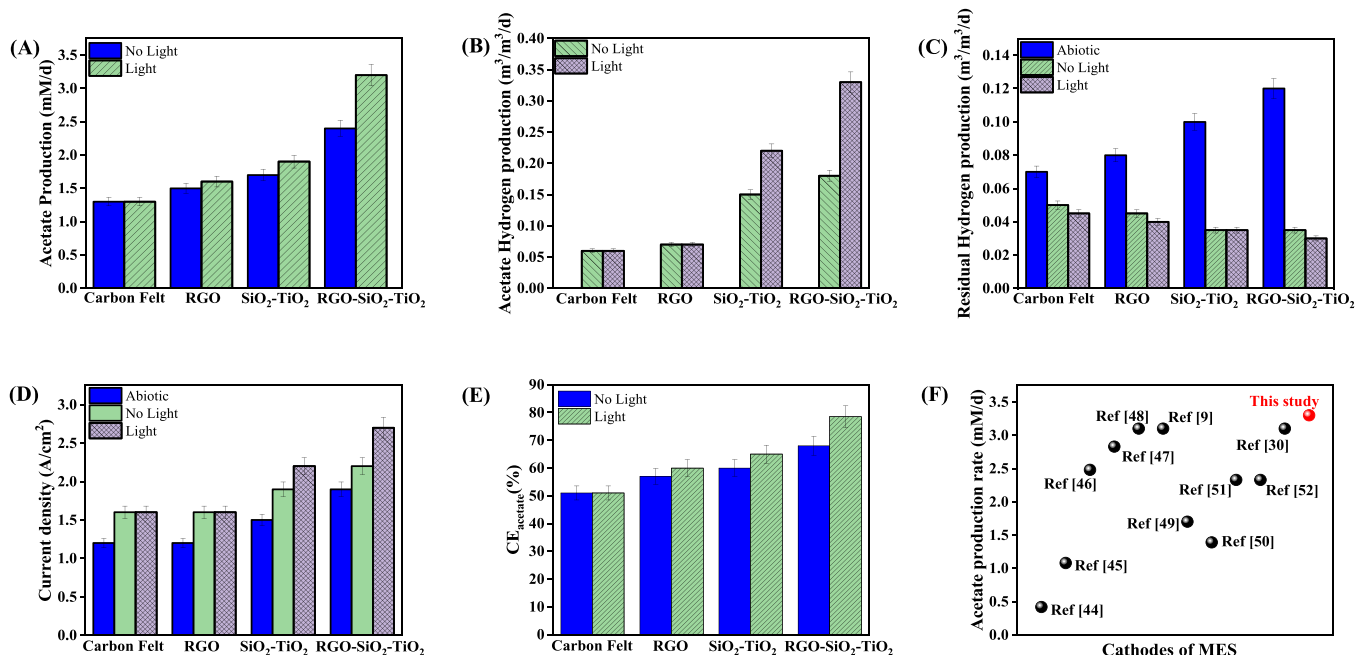
Fig. 5. Comparative (A) Acetate production (B) Acetate hydrogen synthesis (C) Residual Hydrogen synthesis (D) current density and (E) Coulombic efficiency (CE$_{acetate}$) (process time: 12 h).

this system [49]. In all reactors, the inverse correlation between residual hydrogen and Ac production indicates that hydrogen acts as a mediating agent in this system, in agreement with reports on other biohybrid systems (Fig. 5A and B with inset residual hydrogen) [6,15]. Photo-cathodes of the RGO-SiO$_2$-TiO$_2$ n-type produce electrons that can either be accepted by electrotrophs or by H$^+$ for hydrogen evolution (Fig. 5B), both of which are promoted the reduction of IC to Ac (Fig. 5A). It has been earlier reported that such a mechanism works with a different n-type of SC composite (CdS/g-C$_3$N$_4$) operating at cathodic potentials of more negative values from − 1.0 to − 0.9 V [50]. In this case, the

photo-excited electrons drove the reductive degradation of nitro-furazone, while the photo-generated holes at the same time mediated the mineralization of the reductive intermediates.

Electrotrophs microbes immobilized on the photocathodes were not adversely affected by the photocatalytic reaction occurring on the RGO-SiO$_2$-TiO$_2$ semiconductor. Only 2–3% of inactive electrotrophs were observed in the presence of light on RGO-SiO$_2$-TiO$_2$ or SiO$_2$-TiO$_2$ on carbon felt, only 1.3% when no light was present. Similar results were obtained with *Moorella thermoacetica* or *Methanosarcina barkeri* [12,13], which produce methane and Ac using hybrid photo-electrochemical
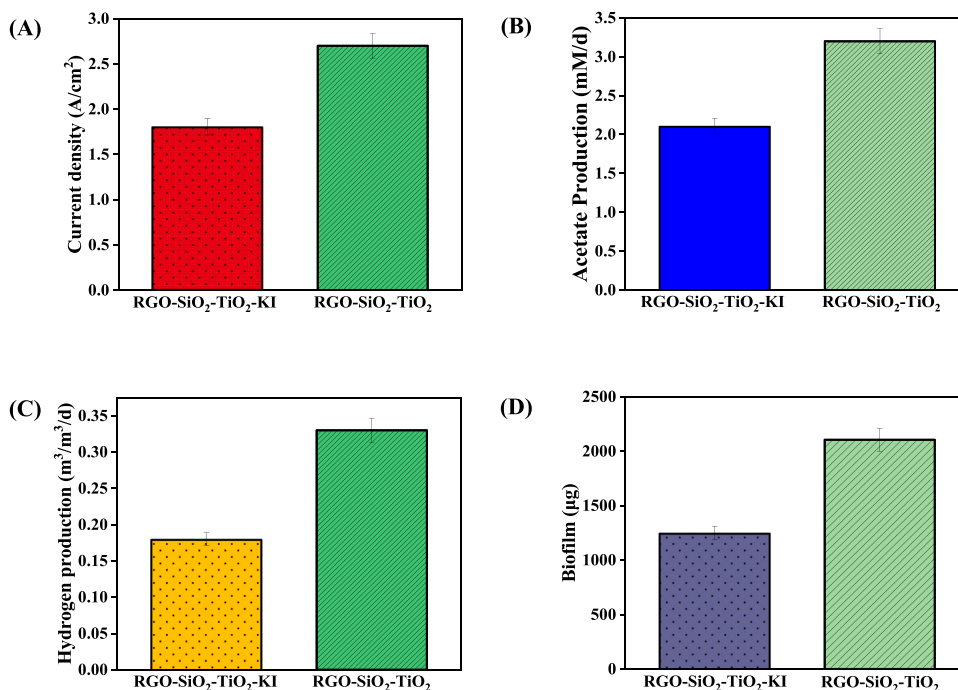

Fig. 6. (A) Comparison is being made between the current density, (B) acetate yield, (C) hydrogen residual, and (D) biomass under the absence or presence of a valence band (VB) hole scavenger of potassium iodide (KI).

processes. In Fig. 5F, we have provided a comparison between the results of our current study and those of previous research in terms of the performance of MES [10,18,21,51–58].

3.2.3. Photocatalytic mechanism of MES with RGO-SiO₂-TiO₂

The mechanism of the photogenerated holes in the semiconductor heterojunction under irradiation was elucidated by incorporating KI as a scavenger for the valence band holes. The inclusion of KI resulted in a decrease in current from 2.7 ± 0.135 A/m² to 1.8 ± 0.09 A/m² (as observed in Fig. 6A), a reduction in acetate production rate from 3.2 ± 0.16 mM/d to 2.10 ± 0.1 mM/d (as depicted in Fig. 6B), and a decrease in the amount of biofilm on the cathode from 2105 ± 105 μg to 1250 ± 62.5 μg (as presented in Fig. 6D). The presence of KI also resulted in reduced hydrogen production, with a decrease from 0.33 ± 0.0165 m³/m³/d to 0.18 ± 0.009 m³/m³/d, as shown in Fig. 6C. This reduction in current (Fig. 6A) along with the lower hydrogen production suggests that the photogenerated holes were trapped by KI and were unable to recombine with the anodic electrons in the external circuit. This indicates that within the SiO₂-TiO₂-rGO heterojunction, the photogenerated holes serve as an additional driving force that effectively traps the electrons in the external circuit, resulting in increased current generation. This outcome is reinforced by the conjecture concerning the function of the photoinduced holes in the decomposition of a dye molecule and the parallel synthesis of molecular hydrogen in a bioelectrochemical system that utilizes a photocathode made up of a heterojunction between graphitic carbon nitride (g-C₃N₄) and bismuth oxybromide (BiOBr) [48] as well as a TiO₂ nanorod array photocathode [59].

Based on the aforementioned evidence, the Bio-photocatalytic mechanism of the MES utilizing SiO₂-TiO₂-rGO was elucidated and summarized in Fig. 7. When the photocatalyst is exposed to visible light, electrons produced by light absorption was transferred from the valence band to the conduction band of SiO₂-TiO₂. At the same time, positively charged holes are generated in the valence band of SiO₂-TiO₂. The incorporation of RGO into the SiO₂-TiO₂ photocatalyst confers several advantages in terms of improved photocatalytic activity. Firstly, the large specific surface area of RGO expanded the light response range, which improved the UV-Vis absorption intensity. This resulted in the provision of more active sites for photocatalytic reactions, ultimately leading to an increase in the light absorption efficiency of the SiO₂-TiO₂ photocatalyst [60]. The overall generation of photogenerated electron holes was observed to increase. Secondly, the introduction of RGO into the

the SiO₂-TiO₂ photocatalyst system served as an electron transfer mediator, facilitated by the π-π conjugation effect of RGO. This mediated electron transfer process significantly accelerated the rate of transfer of photogenerated hole-electron pairs between SiO₂-TiO₂ and RGO, resulting in enhanced electron transfer to hydrogen and direct transfer to microorganisms. The accelerated electron transfer rate was advantageous for the enrichment of electroautotrophic microorganisms in a MES. The presence of a higher reducing power in the system enabled the microorganisms to effectively convert CO₂ into acetate, a valuable metabolic product. This enhanced electron transport rate, facilitated by the introduction of RGO, played a crucial role in promoting the metabolic activity of microorganisms and the overall performance of the MES system. Third, the incorporation of RGO into the SiO₂-TiO₂ photocatalyst was found to significantly enhance the CO₂ adsorption capacity of the composite. This favorable effect on CO₂ adsorption capacity improved the mass transfer of substrates, enabling more efficient reduction of CO₂ by the biocatalyst [10,61]. In summary, the presence of RGO in the SiO₂-TiO₂ photocatalyst led to notable improvements in the separation rate of photogenerated electron-hole pairs, the facilitation of both direct and indirect electron transfer processes, and the acceleration of the mass transfer of substrates. The collective effect of these enhancements significantly improved the overall performance of the photocatalytic system.

3.2.4. Long-term acetate formation kinetics

Acetate production was boosted by the MES's long process (5 days) 8.22 ± 0.30 mM or 2.15 times higher than the control with bare carbon felt electrode as a cathode (Fig. 8A). However, the rate of acetate synthesis gradually dropped as the catholyte's remaining IC was depleted. Moreover, the 3.8 mM/d acetate production rate was 3.3 times that of *Sporomusa ovata* immobilized on surface-modified carbon MES cathodes, without light irradiation (≈ 1.11 mM/d) [8,9]. Still, it was significantly lower than (5.0 mM/d) that was reported using the same species while incubating in a yeast extracting medium with a steady flow of CO₂ [6]. According to (reaction 1), the Ac production reaction consumes hydrogen at a higher rate in RGO-SiO₂-TiO₂ than controls with bare carbon felt cathodes. Therefore, hydrogen concentration was lower than controls with bare carbon felt cathodes which were by the literature that supports other electrochemical reductions that occur without light illumination (Fig. 8B) [6,8]. As observed in Fig. 8B, the residual hydrogen decreased sharply at 1.0 day in correspondence with the maximum rate production of Ac shown in Fig. 8A, indicating that
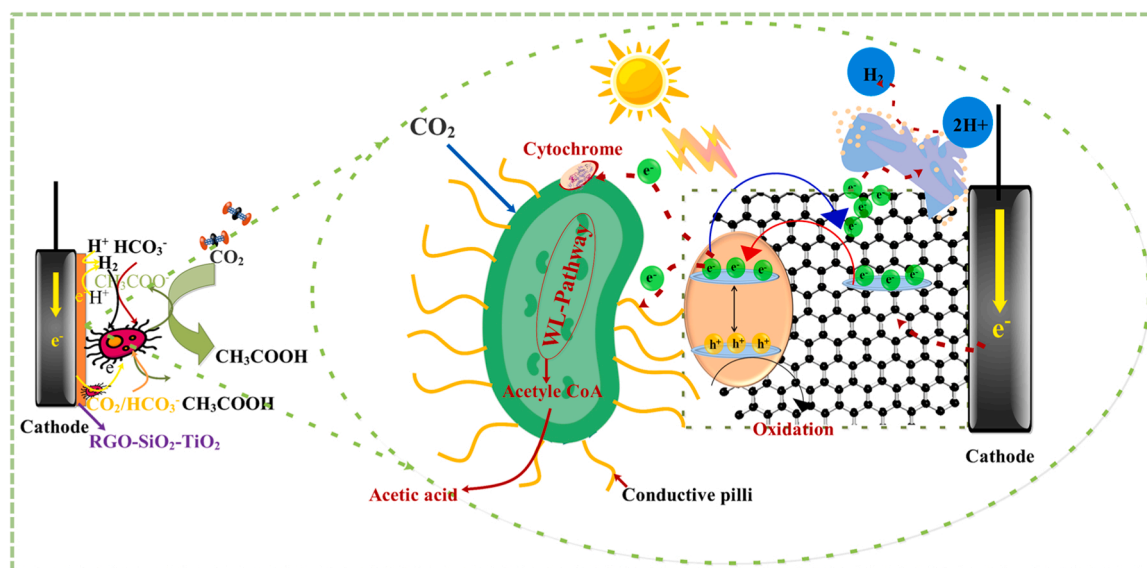

Fig. 7. Photoreduction mechanism of CO₂ to acetate using a mixed culture via the utilization of RGO-doped SiO₂-TiO₂ heterojunction in MES is being investigated.
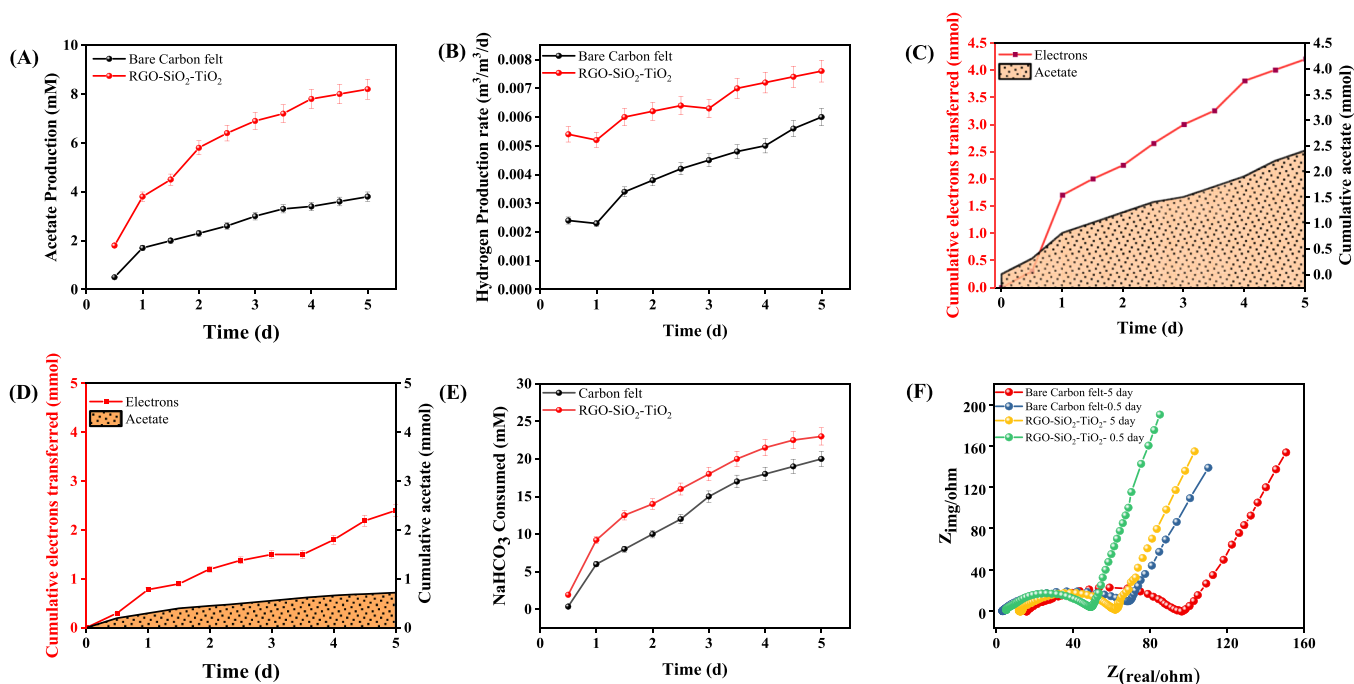
Fig. 8. The progress of time (A) acetate synthesis (B) evolution of hydrogen, (C and D) cumulative electrons transferred for RGO-SiO$_2$-TiO$_2$ and bare carbon felt respectively (E) IC conversion, (F) Nyquist plots of EIS spectra.

photocatalytically generated H$_2$ was efficiently used through photoreduction of protons via the heterojunction valence-band electrons. After 5 days of operation, there was a 42 $\pm$ 2% of CE$_{acetate}$ and a consumption of 95 $\pm$ 2% of the HCO$_3^-$ supplied (Fig. 8C and E), which is much higher than the results of the controls with bare carbon felt cathode was 35 $\pm$ 2% of CE$_{acetate}$ and HCO$_3^-$ consumed 82 $\pm$ 2% as shown in Fig. 8D and E. At a short operating time, 0.5 day CE$_{acetate}$ production of 81 $\pm$ 2% was similar to that obtained in the hybrid system of α-NiS photocatalyst and *Methanosarcina barkeri* for methane production with continuous CO$_2$ supply (74%) [12]. The CE$_{acetate}$ decreased over time with the increase

in internal resistance from 4.5 Ω (R$_s$) and 50.17 Ω (R$_{ct}$) at 0.5 day to 11.8 Ω (Rs) 62.8 Ω (R$_{ct}$) at 5 days (Fig. 6F) caused by exhaustion of the HCO$_3$ supply after 5 days, in accordance with the earlier reported hybrid of *Moorella thermoacetica* and CdS [13]. However, nonstop CO$_2$ sparging may provide sufficient IC for high CE$_{acetate}$, as long as continuous CO$_2$ sparging is carried out throughout the experiment [6,8].

3.2.5. Stability assessment

Multiple batch cycles of the MES assembly system were conducted for every 5.0 days with catholyte refreshment, to evaluate the stability of
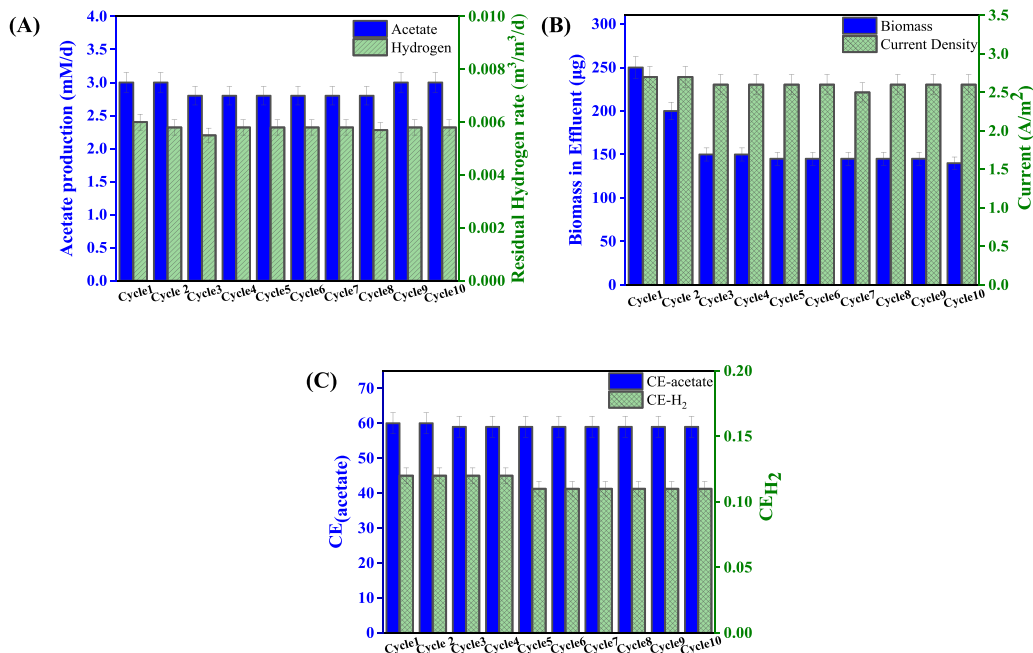

Fig. 9. (A) Acetate production and residual hydrogen (B) Current density and biomass (C) Coulombic efficiency (CE$_{acetate}$) or hydrogen (CE$_{H2}$) varies with the number of cycle (each cycle lasts 120 h).

the Ac production process over a long period of time. In 10 cycles of operations 10 days lasting 1200 h, the Ac production rate (2.8–3.0 mM/d) was similar to the residual hydrogen production rate (0.0050–0.0060 m^3/m^3/d) (Fig. 9A) were noticed. Over the process of 10-cycle operation with $CE_{acetate}$ of 60–59 ± 0.2%, the circuital current stabilized at 2.7–2.5 ± 0.2 A/m^2 (Fig. 9B). In addition, the total number of self-renewing planktonic cells in catholyte effluent varied between 150 ± 10 and 140 ± 10 μg, with a particularly higher value of 250 μg during cycle 1 (Fig. 9C). A steady state value of anerobic cultured microbes was reached in the MES after cycle 2 when the anerobic biofilm first became unstable. Due to the unstable nature of the MES, and as described above and as also proposed by Logan et al. [62], the data at cycle 1–2 cannot represent the long-term performance of the MES. It has been shown for the first time that RGO-SiO$_2$-TiO$_2$ carbon felt photo-cathodes and non-photosynthetic carbon reducing cultured anerobic bacteria can be used as a biocatalyst to produce Ac at a rate of up to 3.20 mM/d ± 0.50 mM/d, with an Ac content of 78 ± 2% $CE_{acetate}$ and a carbon consumption rate of 22 ± 2%, operating at a circuit current of 2.7 A/m^2 under 0.5 d operation time. Furthermore, the elevated Ac production (8.22 ± 0.30 mM) and the almost complete utilization of the IC (95 ± 2%), in the process of 5 days were more beneficial than those in the controls with no light or the carbon felt cathode ($CE_{acetate}$ is 60 ± 0%). The reduced $CE_{acetate}$ is probably the result of a mass transfer restriction, which causes a considerable rise in internal resistance when

low residual IC concentration was present. This problem can be solved by constant CO$_2$ sparging or adding with HCO$_3^-$, which can both effectively deliver a constant supply of the necessary IC to support an unrestrained synthesis of acetic acid or Ac (value added products) [36]. The photocurrent response of RGO-SiO$_2$-TiO$_2$ heterojunction was 2.3 times that of the carbon felt electrode and 1.3 times that of the Si/Ti oxide species, which confirms an improved separation of photo-induced holes and electrons under visible light irradiation as well as synergetic electronic interactions. Furthermore, the EIS showed that RGO-SiO$_2$-TiO$_2$ heterojunctions could separate and transfer photogenerated charge carriers more efficiently than Si/Ti oxides or RGO heterojunctions.

Silicon and Titanium are low-cost oxides that can be easily prepared via in-situ method or recovery easily [22,63]. They perform crucial functions as enzyme activators in numerous bacterial activities, are essential coenzyme building blocks, and are remarkably nontoxic to microorganisms. As an alternative, semiconductor metal oxides containing Cd, Ni, or Cs, such as those used in MES, are mostly toxic to microbes and can even fully dissolve in the catholyte medium after long operation, making them ecologically unfavorable [9,13]. As a consequence of these advantages, the use of RGO-SiO$_2$-TiO$_2$ heterojunctions during the synthesis of Ac from IC reduction in MES, and the self-repair and self-replication mechanisms of cultivated anerobic microbes, is an appealing factor, especially if the procedure is coupled with removal of contaminants from the MES anolyte media [5].
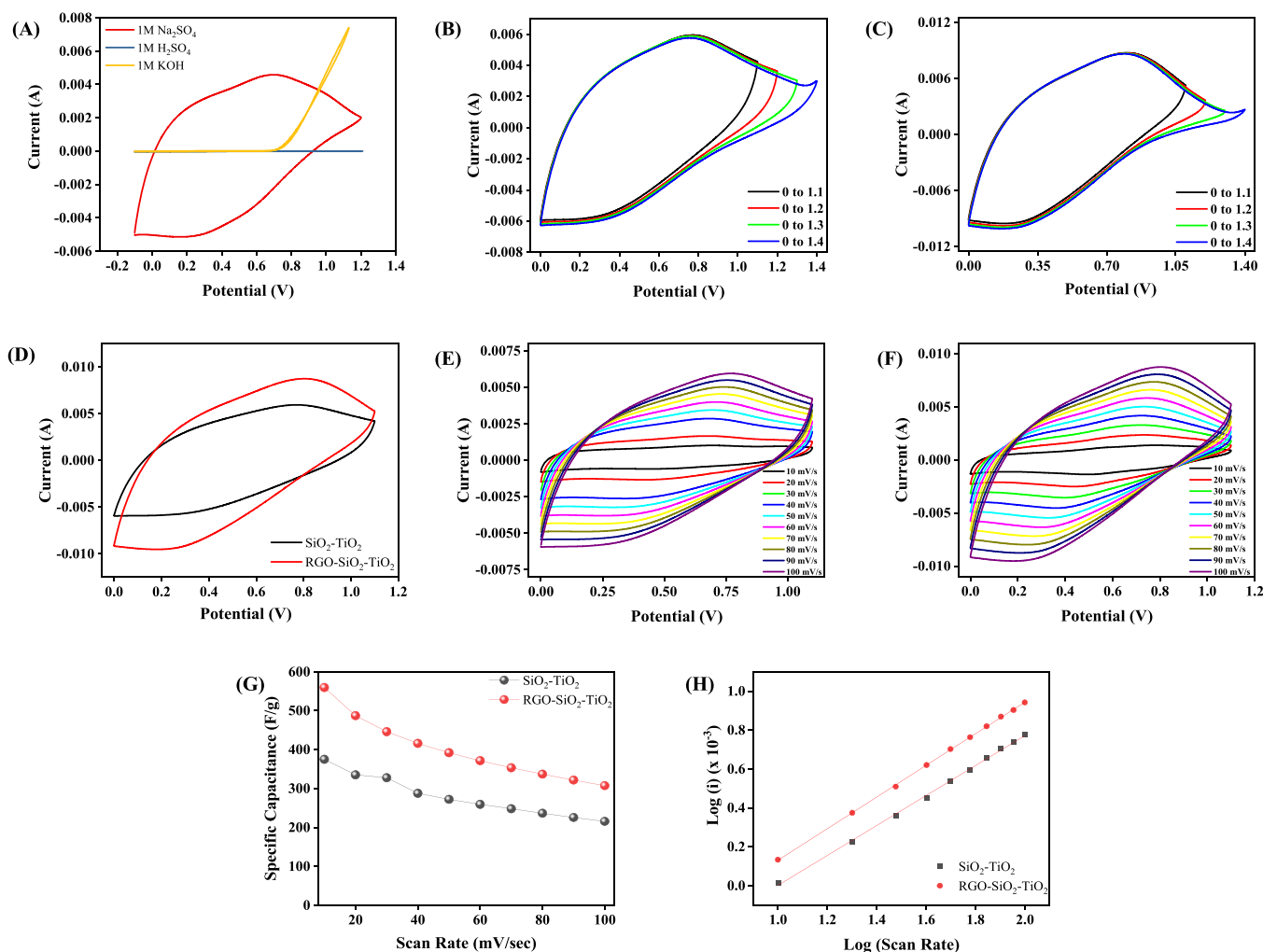
Fig. 10. CV curve of RGO-SiO$_2$-TiO$_2$ NCs in the presence of different electrolyte (A) in the presence of 1 M Na$_2$SO$_4$ electrolyte at varying potential windows (B, C) Comparison of CV at 100 mV/s scan rates for SiO$_2$-TiO$_2$ and RGO-SiO$_2$-TiO$_2$ NCs (D) CV curve of in the presence of 1 M Na$_2$SO$_4$ electrolyte at different scan rates of SiO$_2$-TiO$_2$ NCs and RGO- SiO$_2$-TiO$_2$ NCs ((E, F) Specific capacitance value of SiO$_2$-TiO$_2$ and RGO- SiO$_2$-TiO$_2$ NCs at various scan rates (G) power law dependence of peak current of SiO$_2$-TiO$_2$ and RGO- SiO$_2$-TiO$_2$ NCs (H).

3.3. Three electrode system for supercapacitor

3.3.1. Electrochemical performance

The electrochemical performance of supercapacitors based on RGO-SiO_2-TiO_2 and SiO_2-TiO_2 nanocomposites was evaluated using various techniques, including cyclic voltammetry (CV), galvanostatic charge-discharge (GCD), and electrochemical impedance spectroscopy (EIS). The practicality of the supercapacitor application was assessed by analyzing two parameters, namely different scan rates and charge-discharge cycle numbers, through CV measurements. Additionally, CV was used to identify the oxidation and reduction peaks associated with pseudocapacitance. Before conducting experiments, it is essential to carefully select the appropriate electrolyte and determine the optimal potential window. To evaluate the electrochemical performance of the RGO-SiO_2-TiO_2 and SiO_2-TiO_2 nanocomposites, various electrolytes were employed, including 1 M Na_2SO_4, 1 M KOH, and 1 M H_2SO_4. The voltammograms for these nanocomposites are displayed in Fig. 10A. The cyclic voltammetry and current density values of both RGO-SiO_2-TiO_2 and SiO_2-TiO_2 NCs were found to be superior in 1 M Na_2SO_4 electrolyte. Furthermore, a range of CV curves were obtained at different potential windows between 0 and 1.4 V with a scan rate of 100 mV/s, as illustrated in Fig. 10(B and C). The optimal curve shape was observed up to a potential window of 0–1.2 V, displaying a sharp surge in current response to the working voltage. The tailing observed at the end of the CV curve indicates the onset of oxygen evolution resulting from further voltage elevation up to 1.4 V. To perform a more comprehensive electrochemical analysis of the working electrode, the operating window was adjusted to range from 0 V to 1.2 V. Moreover, the CV curves display the pseudocapacitance behavior of the investigated electrode in the aqueous 1 M Na_2SO_4 electrolyte. To optimize the potential window, a synthesized nanocomposite loaded on a graphite felt substrate was utilized as a working electrode in an aqueous 1 M Na_2SO_4 electrolyte solution with a scanning rate of 100 mV/s. The aim was to adjust the potential window to attain the best possible performance of the electrode.

Comparative CVs of the SiO_2-TiO_2 and RGO-SiO_2-TiO_2 nanocomposites are shown in Fig. 10D at a scan rate of 100 mV/s. Ideally, the CV curve should adopt a rectangular shape with an oblique angle and a small loop, indicating that the electrochemical reaction is reversible, meaning that the forward and reverse reactions occur with equal likelihood. The oblique angle indicates that the reaction rate is fast and the electron transfer is efficient. Furthermore, the small loop indicates that the capacitance of the electrode is low and there is little resistance to electron transfer. Fig. 10D's depiction of the CV curves of SiO_2-TiO_2 and RGO-SiO_2-TiO_2 at a scan rate of 100 mV/s shows that both materials exhibit pseudocapacitive performance due to the presence of SiO_2 containing groups during the redox process. The CV curves of SiO_2-TiO_2 and RGO-SiO_2-TiO_2 NCs were shown in Fig. 10 (E and F) from 10 to 100 mV/s, and it was evident that even at a high scan rate, RGO-SiO_2-TiO_2 (Fig. 10E) maintains a quasi-rectangular shape, highlighting its tremendous rate capacity and kinetic reversibility.

The CV curves show that, at higher current densities, the hysteresis of redox peaks significantly increases along with the scan rate, but the opposite tendency was seen at lower current densities. The electrolyte ions have plenty of time to diffuse and propagate charge with a low current density. On the contrary, as the current density increased, charge propagation slowed as electrolyte ion diffusion decreased. To improve capacitance performance, ions could easily penetrate the pores of electroactive materials at lower current densities. A higher current density, however, led to the opposite result. RGO-SiO_2-TiO_2 or SiO_2-TiO_2 NCs may allow Na^+ ions (from Na_2SO_4 electrolyte solution) to infiltrate the voids. Also, the synthesized nanocomposite seems to have a porous structure, which gives it more active sites for intercalation/deintercalation or charges storage reactions. The comparison CVs of SiO_2-TiO_2 and RGO-SiO_2-TiO_2 NCs at 10 mV/s are shown in Fig. 10(E and F). It demonstrates that RGO-SiO_2-TiO_2 NCs has a relatively high

integrated area than SiO_2-TiO_2. As a result, at 10 mV/s, RGO-SiO_2-TiO_2 NCs illustrates a better specific capacitance (i.e., 559 F/g) than SiO_2-TiO_2, which has 375 F/g. This might be attributable to a decrement in diffusion path length, enhanced feasible surface area, and interactions between RGO and SiO_2-TiO_2 (π- π interaction) that reduce charges' migration lengths.

The determined specific capacitance/scan rates are shown in Fig. 10G. The electrode kinetics at various potentials are investigated to understand better the cause of the high specific capacitance of electrodes made from synthetic nanocomposite materials. It is a well-established fact that the magnitude of the area under the cyclic voltammetry curve is directly proportional to the scan rate. This correlation between the two parameters can be attributed to the joint contribution of the capacitive and intercalation effects. The interplay of these electrochemical phenomena leads to the overall charge that gets accumulated in the electrode. The two processes that make up the capacitive process are surface redox and the ions adsorption/desorption reaction, or the development of an electric double layer at the electrode/electrolyte interface. Capacitive mechanisms are driven by surface redox and ion adsorption/desorption (or EDLC generation) reactions at the electrode/electrolyte interface.

The specific capacitances of the SiO_2-TiO_2 and RGO-SiO_2-TiO_2 NCs were determined to be 599 and 474 F/g, respectively. Due to the presence of RGO in the SiO_2-TiO_2 backbone, RGO-SiO_2-TiO_2 NCs displayed a higher capacitance than SiO_2-TiO_2 NCs at a current density of 4 A/g (Fig. 11A). Furthermore, incorporating RGO in the SiO_2-TiO_2 matrix might improve energy storage by lowering electrode inner resistance and facilitating charge transfer. Fig. 11(B and C) depicts the charging-discharging curves of SiO_2-TiO_2 and RGO-SiO_2-TiO_2 NCs at different current densities ranging from 4.0 to 20.0 A/g. The capacitance decreases with increasing current density. When the current density is lower, the electrolyte ions can diffuse entirely into the inner active sites, increasing capacitance. Increasing the current density resulted in the opposite results, with the specific capacitance decreasing with an increase in current density.

RGO-SiO_2-TiO_2 NCs electrodes were tested for their specific capacitance at different current densities. It was observed that the gravimetric capacitance (Fig. 11D) decreased with increasing current density from 4, 6, 8, 10, 12, 15 and 20 A/g to 599, 480, 458, 435, 403, 381, 328 F/g for RGO-SiO_2-TiO_2 NCs and 474, 375, 347, 328, 303, 298, 267 F/g for SiO_2-TiO_2 NCs. While the current density was raised from 4 to 20 A/g, the capacitive retention of SiO_2-TiO_2 and RGO-SiO_2-TiO_2 NCs were 54% and 57%, respectively.

The predicted capacitance values decreased at the highest charge-discharge current densities. At increasing current densities, the pseudocapacitive behavior of the electrolyte-electrode interface is impeded by an increase in resistance and a too-short period. It may be due to a reduced diffusion of the electrolyte ions that specific capacitance declines at high scan rates. Due to the time constraint, the high rate of charge-discharge typically restricts ionic mobility in the electrolyte through diffusion. This is due to charge storage being used on the active exterior surface, which results in decreasing electrochemical activity. The increased conductivity of the RGO-SiO_2-TiO_2 NCs offers a path for electron transport, which is helpful for fast charging and discharging. Furthermore, increased conductivity may reduce the electric resistance for electron transfer, improving energy functioning even further. These results demonstrate the RGO-SiO_2-TiO_2 NCs nanostructure's remarkably high charge-discharge rated capacitance. Finally, the electrochemical stability of RGO-SiO_2-TiO_2 NCs is investigated after they have been subjected to a total of 4000 galvanostatic charge-discharge cycles. In order to evaluate the performance, a high current density of 10 A/g was maintained within a potential window ranging from 0 V to + 1.2 V (Fig. 11E).

One effective approach to assessing the internal resistance of the electrode material and the electrolyte ion transport within the supercapacitor is the electrochemical impedance spectrum (EIS). The RGO
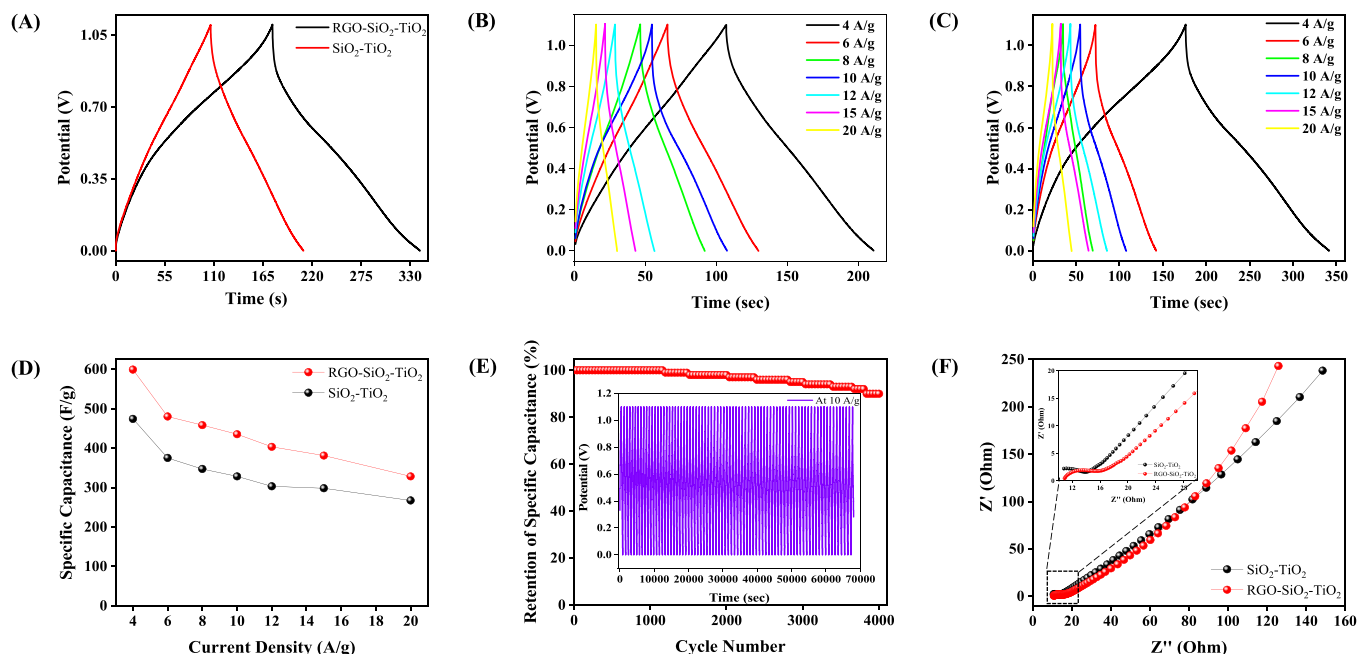
Fig. 11. Galvanostatic discharge curves of SiO$_2$-TiO$_2$ and RGO-SiO$_2$-TiO$_2$ NCs at 20 A/g (A) Galvanostatic discharge curves of SiO$_2$-TiO$_2$ and RGO-SiO$_2$-TiO$_2$ NCs at different current densities (B, C) Specific capacitance value of SiO$_2$-TiO$_2$ and RGO-SiO$_2$-TiO$_2$ NCs at various current densities (D) Capacitive retention values of RGO-SiO$_2$-TiO$_2$ NCs at 10 A/g scan rate for 4000 cycles (inset shows the corresponding CD curves) (E) Electrochemical impedance spectrum (EIS) of SiO$_2$-TiO$_2$ and RGO-SiO$_2$-TiO$_2$ NCs (F).

plays a role in the nanocomposite electrodes in three different ways, which are as follows: (i) The large surface area and inherent capacitance of RGO lead to the enhancement of specific capacitance. (ii) The introduction of RGO increased the conductivity of the RGO-SiO$_2$-TiO$_2$ NCs, as evidenced by the EIS data in Fig. 11F. The sp^2-hybridized structure of RGO serves as the foundation for its conductive mechanism. As a result, there is less resistance when electrons move between the SiO$_2$-TiO$_2$ and RGO. (iii) RGO increases the number of reactive sites for SiO$_2$-TiO$_2$, resulting in an effective channel for electron transport between RGO and SiO$_2$-TiO$_2$ NCs. Fig. 11F demonstrates that the Nyquist impedance plots of SiO$_2$-TiO$_2$ and RGO-SiO$_2$-TiO$_2$ electrodes in 1 M Na$_2$SO$_4$ electrolyte comprise semicircles in the high-frequency area and a curving line in the low-frequency zone. The charge transfer impedance at the electrode/electrolyte interface and the pseudocapacitive nature of the electrode can be observed in the plots as a depressed semicircle in the high-frequency region for all electrodes. At a high frequency of 0.1 kHz, the intersection of a semicircle with the real impedance axis (Z$_0$) yields the equivalent series resistance (ESR), which comprises the resistance of the electrolyte separator and the resistance of the current collectors. The series resistance (R$_s$) caused by the electrolyte solution, which is 10.80 Ω and 10.91 Ω, respectively, for RGO-SiO$_2$-TiO$_2$ NCs and SiO$_2$-TiO$_2$ NCs, can be shown to be nearly consistent across the entire potential window. When used in parallel with a constant phase element, charge transfer resistance (R$_{ct}$) has a minimum value at OCP but significantly varies with applied voltage. On the other hand, the wide semicircle shows a high degree of charge transfer resistance between the electrode materials and the electrolyte solution at the electrode/electrolyte interface.

Current exchange density is another way to represent an electrode's charge transfer resistance (R$_{ct}$). Express using the following formula (Eq. 8) [64]:

$$R_{ct} = \frac{RT}{iF} \tag{8}$$

Where R is the gas constant (J mol^{-1} K^{-1}), T is the temperature (Kelvin), i is the current exchange density in Ampere, and F is the Faraday constant (coulomb/mol).

The abovementioned equation may thus be used to determine the

charge transfer resistance (R$_{ct}$) at a reversible potential. A drop in current exchange density due to a Faradic response rate might illuminate the rise in charge transfer resistance (R$_{ct}$). The R$_{ct}$ values for the RGO-SiO$_2$-TiO$_2$ NCs and SiO$_2$-TiO$_2$ NCs electrodes are found to be 6.23 Ω and 10.55 Ω, respectively (Fig. 11F). The electrode's performance has been enhanced by the reduction of internal resistance caused by the encapsulation of SiO$_2$-TiO$_2$ NCs inside the RGO, as shown by the lowest R$_{ct}$ value for RGO-SiO$_2$-TiO$_2$ NCs. Warburg impedance in the low-frequency range of nanocomposite electrodes is shown as a sloping line with 45-degree angles in the EIS plots. This impedance is ascribed to the diffusion of Na$^+$ ions into the bulk of the electrode nanomaterials. The ternary electrode's Warburg impedance has minimal ionic diffusion resistance and pure capacitance behavior, which is verified by CV data. RGO-SiO$_2$-TiO$_2$ NCs exhibit low ionic diffusion resistance and R$_{ct}$, which results in shortened electron diffusion paths and improved electron transfer.

The Randles-Sevcik formula (Eq. 9) was used to compute the diffusion coefficient D$_0$ for the constructed electrode in the Na$_2$SO$_4$ medium [65,66].

$$I_p = \left(2.687 \times 10^5 \right) n^{\frac{3}{2}} ACD_0^{\frac{1}{2}} \vartheta^{\frac{1}{2}} \tag{9}$$

where I$_p$ is the peak current position, n is the number of electrons transferred in the redox reaction, A is the effective electrode area of the working electrode in cm^2, C is the concentration of the diffusing species in the bulk of the electrolyte, and v is the voltage scan rate.

The equation mentioned above estimates the diffusion coefficient of electrolyte ions at the interfacial area to be 7.31×10^{-15} cm^2/s for the SiO$_2$-TiO$_2$ electrode and 1.60×10^{-14} cm^2/s for the RGO-SiO$_2$-TiO$_2$ electrode, respectively. Due to the layered structure with the large interlayer spacing, the RGO-SiO$_2$-TiO$_2$ NCs is believed to provide a significantly larger surface area and more active sites for ion transport resulting in improved performance.

3.3.2. Charge storage mechanism of RGO-SiO$_2$-TiO$_2$ NCs

The current obtained from cyclic voltammetry is governed by a mathematical relationship known as Power's law, which describes how the scan rate impacts the current. This is expressed in Eq. 10, which

quantifies the exact nature of this dependence [64].

$$I = a\vartheta^b \tag{10}$$

The adjustable parameters a and b play a crucial role in describing the behavior of the system with respect to the scan rate (ν/s). The slope of the linear fit in the log I vs. log ν plot at a specific potential (V) enables the calculation of the value of b. When the process is dominated by diffusion, such as in the case of ion intercalation into electrodes, b takes a value of 0.5. However, for capacitive or non-diffusive controlled processes, the value of b is 1. This information is particularly useful in understanding and characterizing electrochemical systems. When calculating the b value for SiO$_2$-TiO$_2$ and RGO-SiO$_2$-TiO$_2$ nanocomposite, the current log is plotted against the voltage scan rate log for each data point. This allows the b value to be determined. The resulting b-values for SiO$_2$-TiO$_2$ and RGO-SiO$_2$-TiO$_2$ nanocomposite are 0.78 and 0.82, respectively, as shown in Fig. 10H. The high specific capacitance value observed in nanomaterials may be attributed to the nanosize effect of the particles and the significantly accessible surface of the electrode materials, which could be explained by either a capacitive process or a fast-redox reaction process that is free from any diffusion limitations. These types of nanomaterials have been referred to as "extrinsic pseudocapacitors".

A representation of the logarithmic breakdown of Eq. 11, which separates the aνb term into two distinct components, is illustrated in Fig. 10H (in above section) [64].

$$I = k_1\nu + k_2\nu \tag{11}$$

Through the determination of k1 and k2, it becomes feasible to differentiate and assess the relative importance of the capacitive mechanisms, including electrical double-layer capacitance (EDLC) and pseudocapacitance, and the diffusion-limited processes.

In Fig. 10G, it can be observed that the specific capacitance of RGO-SiO$_2$-TiO$_2$ NCs and SiO$_2$-TiO$_2$ attains the highest value at a scan rate of 10 mV/s, and the lowest value at 100 mV/s. This may be attributed to the saturation of the electrolytic ions at the outer surface of the electrode. As depicted in Fig. 10G, the specific capacitance of SiO$_2$-TiO$_2$ and RGO-SiO$_2$-TiO$_2$ NCs decrease by approximately 57% and 55%, respectively, when the scan rate is increased from 10 mV/s to 100 mV/s. The specific capacitance of RGO-SiO$_2$-TiO$_2$ NCs may be attributed to a number of factors, such as (i) the high surface area of RGO-SiO$_2$ present in the NCs, (ii) the high electron density of RGO-TiO$_2$ in RGO-SiO$_2$-TiO$_2$ NCs, (iii) the strong interaction between RGO and SiO$_2$-TiO$_2$ NCs, and (iv) the gradual wrapping of RGO surfaces on SiO$_2$-TiO$_2$, resulting in a structural enhancement for improved electrolyte accessibility.

At low scan rates, the high specific capacitance values observed can be attributed to active inner sites and a fast-faradaic transition, while the capacitance value is reduced at high scan rates due to sluggish proton diffusion across the electrode. The RGO-SiO$_2$-TiO$_2$ NCs electrodes exhibit two distinct capacitive charge storage mechanisms.

(i) The intercalation of alkali metal ions, such as Na$^+$ from the Na$_2$SO$_4$ electrolyte, occurs when the RGO-SiO$_2$-TiO$_2$ NCs electrode is reduced, whereas de-intercalation occurs when it is oxidized. Eq. 12 illustrates a potential reaction mechanism:

$$RGO - SiO_2 - TiO_2 + Na^+ + e^- \leftrightarrow RGO - SiO_2 - TiO_2 - Na \tag{12}$$

(ii) The RGO-SiO$_2$-TiO$_2$ NCs are employed in a capacitive charge storage mechanism that utilizes a surface process to adsorb and de-adsorb Na$^+$ alkali metal ions. This second mechanism is characterized by the following reaction mechanism (Eq. 13):

$$(RGO - SiO_2 - TiO_2)_{surface} + Na^+ + e^- \leftrightarrow (RGO - SiO_2 - TiO_2 - Na^+)_{surface} \tag{13}$$
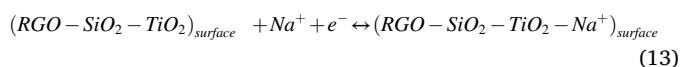
The capacitive charge storage mechanism in TiO$_2$, which has a crystalline structure, is predominantly achieved through intercalation/

deintercalation, while in RGO-SiO$_2$, which has an amorphous structure, it is achieved through surface adsorption/desorption. In the latter case, the specific capacitance is dependent on the interaction between RGO and SiO$_2$-TiO$_2$ nanocomposites. Thus, the surface adsorption/de-adsorption process plays a crucial role in the capacitive charge storage mechanism of RGO-SiO$_2$-TiO$_2$ NCs, and the specific capacitance is influenced by the synergistic effect of the RGO and SiO$_2$-TiO$_2$ nanocomposite. The redox process in the nanostructured RGO-SiO$_2$-TiO$_2$ matrix is mainly controlled by the adsorption and desorption of Na+ on its surface. The lack of redox peaks in all the CV curves indicates that the electrode was charged/discharged at a nearly constant rate throughout the CV cycle. To gain more knowledge about electrochemical activity, a technique similar to Trassati's was adopted to establish a link between the scan rate and specific capacitance [67,68]. The CV analysis of RGO-SiO$_2$-TiO$_2$ demonstrated shapes that were not quasi-rectangular, implying that both double-layer capacitance and pseudocapacitance mechanisms were contributing to the overall capacitance of the electrode. To distinguish the specific contributions of each mechanism, Trassati's method was utilized. This method suggests that the total capacitance of the electrode can be divided into two parts: C$_{inner}$, which represents the redox processes happening within the bulk of the electrode, and C$_{outer}$, which represents the electrostatic adsorption mechanism at the outer surface of the electrode. Its analysis indicates that the mechanism of charge storage is dependent on the scan rates, as shown in Fig. 12 A-G. By calculating the redox reaction on the surface and the accumulation of charge between the active material and the electrolyte, Eq. (14) can be obtained.

$$C_{Total} = C_{inner} + C_{outer} \tag{14}$$

At higher scan rates, the capacitance of the electrode is dominated by the outer surface where the total capacitance (C$_{Total}$) is made up of the double-layer capacitance (C$_{dl}$) and pseudocapacitance (C$_{pseudo}$). As a result, it is only at lower scan rates that a precise evaluation of both the inner and outer charge contributions can be made [64].

The contribution of total capacitance or outer charge can be estimated using the Eqs. (15 and 16).

$$\frac{1}{\sqrt{\vartheta}} = C_{Total} + \sqrt{\vartheta} \tag{15}$$

$$\vartheta = C_{inner} + \frac{1}{\sqrt{\vartheta}} \tag{16}$$

where the scan rate ϑ is a factor in this equation, and in this study, the total capacitance (C$_T$) was obtained by fitting C$^{-1}(\vartheta)$ vs. $\sqrt{\vartheta}$, which resulted in a value of 599.62 F/g (depicted in Fig. 12C). By plotting C vs $\vartheta^{-0.5}$, (as shown in Fig. 12D), the amount of charge stored on the electrode material's outer surface can be determined by extrapolating the graph to the y-axis. The y-axis intercept plot at $\sqrt{\vartheta} \rightarrow 0$ depicts the upper limit of the maximum specific capacitance potential due to the uncontrolled diffusion of ions, resulting in the experimental data deviating from a linear trend due to ohmic drop and irreversible redox reactions. Therefore, selective fitting of the data at lower scan rates allowed us to extrapolate the fitted curve to determine the maximum specific capacitance (C Total) for RGO-SiO$_2$-TiO$_2$ NCs (as shown in Fig. 12E). Extrapolating the linear plot of C_{Total} vs $\sqrt{\vartheta}$ y-axis intercept at $\sqrt{\vartheta} \rightarrow 0$, determines the highest specific capacitance value due to uncontrolled ions diffusion, which explains the lowest possible specific capacitance value. Subsequently, a linear relationship between C_{Total} vs $\frac{1}{\sqrt{\vartheta}}$ plot reveals the following findings.

At higher scan rates ($\vartheta \rightarrow \infty$), controlled ions diffusion into the electrode pores may occur, thereby contributing to the specific capacitance. The RGO-SiO$_2$-TiO$_2$ nanocomposite electrode's total specific capacitance (CT) and outer surface specific capacitance (C$_{out}$) were estimated to be 479.42 F/g. The specific capacitance of the inner surface
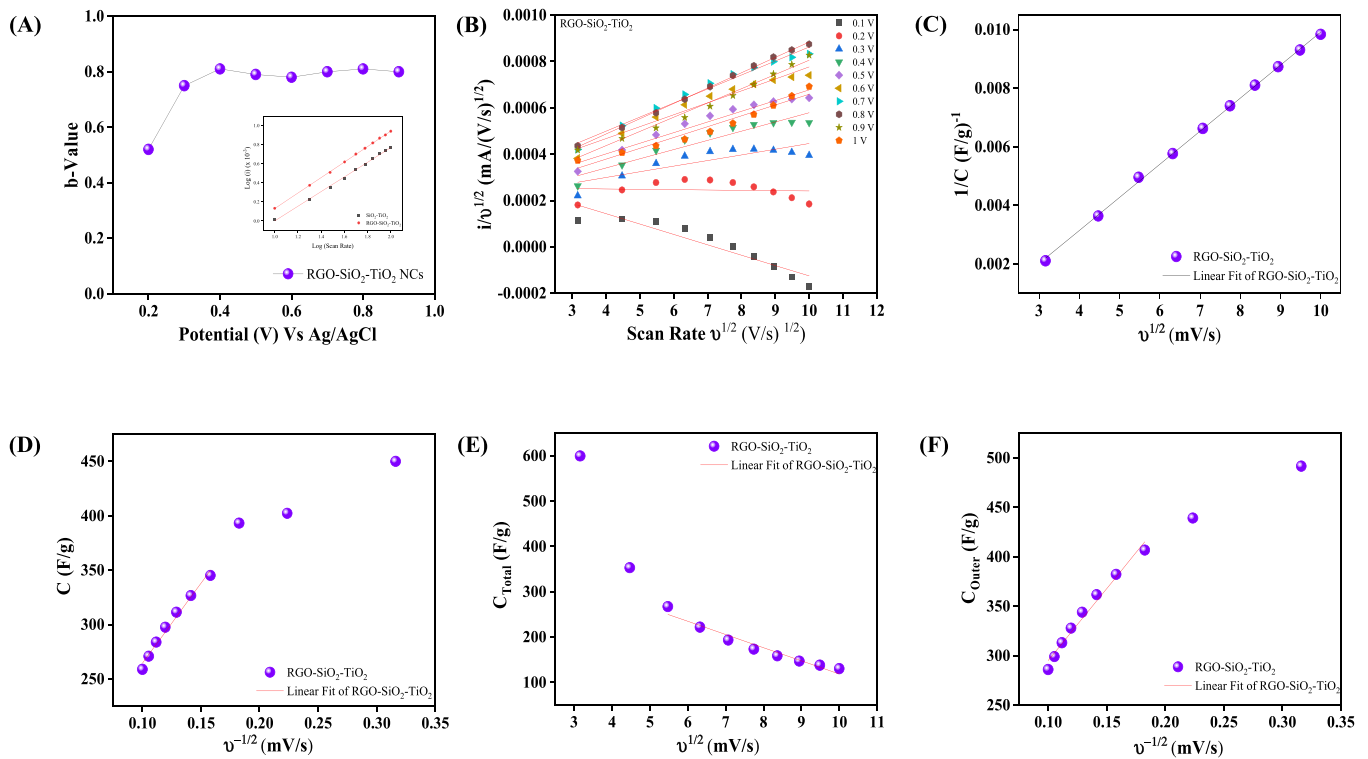
Fig. 12. (A) b-values as a function of potential sweeps for RGO-SiO$_2$-TiO$_2$ NCs. (B, C) Square root of scan rate ($\nu^{1/2}$) vs i/$\nu^{1/2}$ graph for k_1 and k_2 determination for RGO-SiO$_2$-TiO$_2$ NCs and SiO$_2$-TiO$_2$ (D) Charge storage mechanism by Trasatti method, Plot of reciprocal of capacitance (C^{-1}) vs square root of scan rate ($\nu^{1/2}$) (E) Plot of C (C/g) vs the reciprocal of square root of scan rate ($\nu^{-1/2}$) by following the power law dependence (F) Specific capacitance vs $\nu^{-1/2}$.

(C_{in}) was estimated to be 120.20 F/g by subtracting C_{out} from C_T, as shown in Fig. 12F. This suggests that the outer surface of the RGO-SiO$_2$-TiO$_2$ nanocomposite electrode contains a significant number of active sites. Moreover, the specific capacitance value is mainly derived from the contribution of the external sites, indicating that pseudocapacitance plays a vital role in the charge storage mechanism. Based on the results

presented in Fig. S5, it can be inferred that pseudocapacitance contributes to approximately 18.68% of the total capacitance, while double layer capacitance accounts for only 81.31%. These findings demonstrate that the RGO-SiO$_2$-TiO$_2$ nanocomposites possess a high pseudocapacitive contribution and that their charge storage mechanism is significantly influenced by pseudocapacitance.
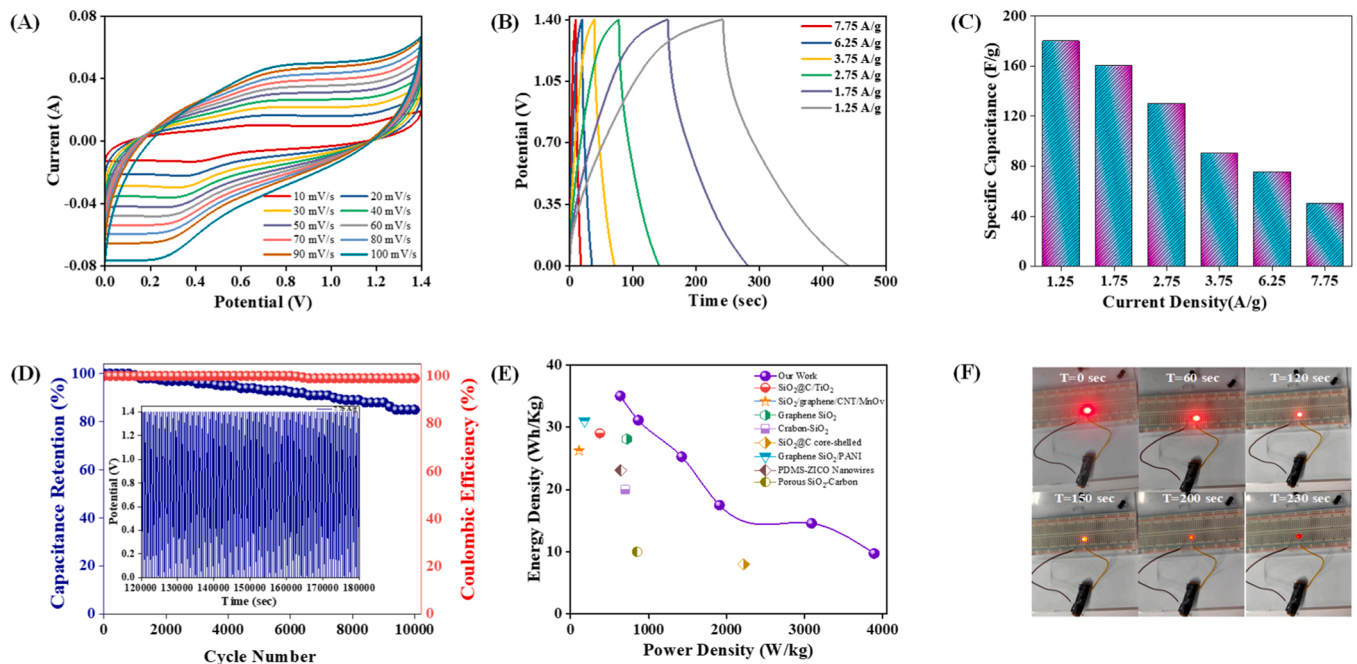

Fig. 13. (A) CV curves of device (D) GCD curves, (E) relationship between specific capacitance and current densities, (F) Cycling stability at 10 A/g of SSD (G) Ragone plots and (H) Digital photo of assembled devices in series lighting up a LED indicator.

3.4. Pouch type RGO-SiO$_2$-TiO$_2$ NCs based supercapacitor device

To assess the energy storage capability of the supercapacitor, we created a symmetrical supercapacitor device (SSD device). Since the electrodes of the device were symmetrical, there was no need to maintain a charge balance. Fig. 13A illustrates the CV profiles collected at various scan rates ranging from 10 to 100 mV/s, which demonstrate that the device maintains its symmetry and structure even under high scan rates. The CV profiles suggest that the capacitance of the EDLC plays a significant role in the device's performance.

In addition, the GCD curves obtained from the device exhibited exceptional performance over the potential range of 0–1.4 V, as illustrated in Fig. 13(A and B), providing clear evidence of its remarkable functionality. The charge-discharge curves exhibited by the RGO-SiO$_2$-TiO$_2$ nanocomposites display a notable capacity for storing charge and demonstrate good reversibility in the SSD device. This is evident in the symmetric nonlinear nature of the curves. A thorough examination of the CV curves revealed that the charge storage mechanism in the nanocomposite is influenced by both surface-controlled and diffusion processes. At high scan rates, the CV curves exhibited by the RGO-SiO$_2$-TiO$_2$ nanocomposites adopt a quasi-rectangular shape. This distinctive shape is indicative of the fast adsorption and desorption of charges from the surface of the nanocomposites, which gives rise to high voltage rates. The observed behavior further underscores the potential of RGO-SiO$_2$-TiO$_2$ nanocomposites for use in high-performance energy storage applications. However, even under high scan rates, the CV plots displayed remarkable consistency, indicating a desirable degree of structural stability and reversibility. Notably, the CV curves exhibited negligible variations, despite the application of high scanning rates ranging from 60 to 100 mV/s. This observation suggests that the RGO-SiO$_2$-TiO$_2$ nanocomposite-based SSD possessed an improved rate capability, making it suitable for high-power applications. In Fig. 13B, it can be observed that the RGO-SiO$_2$-TiO$_2$ nanocomposite-based SSD manifests a discharge-specific capacitance. The discharge profile of the GCD plots was utilized to quantify this attribute at varying current densities ranging from 1.25 to 7.75 A/g. By analyzing the GCD curves depicted in Fig. 13C, the gravimetric capacitances were determined to be at 1.25 A/g (180 F/g), 1.75 A/g (160 F/g), 2.75 A/g (130 F/g), 3.75 A/g (90 F/g), 6.25 A/g (75 F/g) and 7.75 A/g (50 F/g) respectively. The SSD incorporating RGO-SiO$_2$-TiO$_2$ nanocomposites displayed Columbic efficiencies in the range of 82–89% at various current densities ranging from 1.25 to 7.75 A/g. Although the GCD plots exhibited shorter discharge times at lower current densities, a more intricate analysis revealed that the SSD device exhibited excellent charge-transfer performance at current densities ranging from 1.25 A/g to 3.75 A/g. However, this performance was compromised at current densities lower than 6.25 A/g. The observed phenomenon can be ascribed to the sluggish and irreversible Faradaic reactions that occur at lower applied currents. This phenomenon is exacerbated by the elevated occurrence of side reactions at lower current densities relative to higher ones. The empirical evidence lends support to the hypothesis that the electrode material's ability to endure higher current densities is a crucial determinant of its electrochemical performance. This conjecture is bolstered by the favorable performance of the current SSD utilizing the RGO-SiO$_2$-TiO$_2$ nanocomposite electrode, which exhibited an excellent capacity to withstand high current densities. The observed augmentation in Columbic efficiency and the reduction in discharge time at elevated current densities signify promising supercapacitor traits, including excellent energy storage capacity and rapid power dissipation capabilities. The RGO-SiO$_2$-TiO$_2$ nanocomposite-based SSD was subjected to up to 10,000 cycles, and the results (Fig. 13D) reveal an 84% retention capability. However, the capacitance experienced a drastic decline when the active components disengaged from the electrode surface. Despite this, there was a significant decrease in capacitance when the active components detached from the electrode surface. When conducting cycling stability tests of the RGO-SiO$_2$-TiO$_2$ nanocomposite-based SSD,

within the last 200 cycles at 7.75 A/g current density, the symmetrical chronopotentiometry curves showed a linear voltage variation over time (as seen in the inset of Fig. 13D). The electrodes' surface wettability was observed to increase the ion diffusion in the electrode microstructure, which led to an increased penetration depth and a reduced ion migration path. In addition, the RGO-SiO$_2$-TiO$_2$ nanocomposites have a highly porous structure that allows for a greater influx of electrolyte ions into the electrode, thereby enhancing the material activation process. The mechanism responsible for this diffusion enhancement has been found to effectively activate a larger number of sites, thereby promoting the redox reaction. This, in turn, leads to a significant improvement in the cycle stability of the specific capacitance, which can sustain up to 84% of its initial capacitance despite a decline subsequent to reaching its maximum value. However, the detachment of active components from the electrode surface causes an abrupt decrease in capacitance.

The energy and power density of the SSD device were computed by using the GCD plots as a reference. A typical Ragone plot was established, as depicted in Fig. 13E. The results indicated that our SSD device possesses the ability to produce energy densities of 35 Wh/kg, 31.11 Wh/kg, 25.27 Wh/kg, 17.50 Wh/kg, 14.58 Wh/kg, and 9.72 Wh/kg, even at a high-power density of 0.63 kW/kg, 0.86 kW/kg, 1.42 kW/kg, 1.90 kW/kg, 3.08 kW/kg, and 3.88 kW/kg, respectively. These values are higher compared to other similar supercapacitor devices, such as SiO$_2$ @C/TiO$_2$//AC (29 Wh/kg and 375 W/kg)[28], SiO$_2$/Graphene/CNT/MnOv//AC (26.25 Wh/kg and 110 W/kg)[69], Carbon-SiO$_2$//AC (20 Wh/kg and 700 W/kg)[70], SiO$_2$ @C Core-Shell//AC (8 Wh/kg and 2215 W/kg)[71], Graphene SiO$_2$/PANI (31 Wh/kg and 180 W/kg)[72], PDMS-ZiCO Nanowire//AC (23.1 Wh/kg and 640 W/kg)[73], and Porous SiO$_2$-Carbon (10 Wh/kg 850 W/kg)[74]. In addition, Fig. 13F shows the schematic fabrication of the SSD device and its illumination of light-emitting diodes for 230 s

4. Conclusions

Pluronic F-68 was the key ingredient in the synthesis of RGO, mesoporous SiO$_2$, and TiO$_2$ nanocomposites, which were made using a sol-gel co-condensation approach. Various analytical techniques were employed to investigate the structure and composition of the resulting RGO-SiO$_2$-TiO$_2$ nanocomposites, and the electrochemical properties of the nanocomposites were investigated. The results showed that the RGO-SiO$_2$-TiO$_2$ nanocomposites were superior to Si-Ti oxides in catalyzing the electroreduction of CO$_2$ through microbial electrosynthesis (MES) and high-performance supercapacitor electrodes. Upon optimizing the mass loading of the RGO-SiO$_2$-TiO$_2$ electrode and the RGO/Si-Ti ratio, the synthesized nanocomposite displayed a consistent and reversible photo-current response that was 1.4 times higher than the response observed with Si-Ti oxides. The hybrid RGO-SiO$_2$-TiO$_2$ heterojunction, along with mixed microbe cultivation, produced acetate with a high CE$_{acetate}$ of 78 ± 5%. This nanocomposite also enhanced the current and capacitance of the system, which led to a boost in CO$_2$ reduction rates.

The RGO-SiO$_2$-TiO$_2$ NCs electrode also exhibited higher supercapacitance and retained capacitance stability after 4000 cycles at 10 A/g (92%). The integration of RGO structure with SiO$_2$-TiO$_2$ NCs through π π -conjugated networks enhanced electrical conductivity, leading to improved cyclic stability, highly accessible surface area, and ionic transport. The fabricated Supercapacitor device using RGO-SiO$_2$-TiO$_2$ NCs demonstrated the ability to undergo up to 10,000 consecutive charge-discharge cycles, exhibiting 84% specific capacitance retention after cyclic stability with a maximum energy density of 35 Wh/kg at 630 W/kg power density. Overall, the synthesized RGO-SiO$_2$-TiO$_2$ NCs nanocomposites exhibit promising properties for utilization as an energy storage medium for the reduction of CO$_2$ into valuable products and for electricity harvesting through the use of supercapacitor devices. These findings offer a potential solution for addressing the current energy and environmental crisis.

CRediT authorship contribution statement

Abdul Hakeem Anwer: Conceptualization, Writing – original draft, Writing – review & editing, Methodology. **Mohd Shoeb:** Software, Conceptualization, Writing – review & editing. **Fouzia Mashkoor:** Writing – review & editing. **Aleesha Ali:** Software, Writing – review & editing. **Sumairah Kareem:** Data curation, Software, review & editing. **Mohd Zahid Ansari:** Software, Writing – review & editing. **Jang Min Park:** Data Curation, Software. **Changyoon Jeong:** Writing – original draft, Writing – review & editing, Supervision.

Declaration of Competing Interest

The authors declare that they have no known competing financial interests or personal relationships that could have appeared to influence the work reported in this paper.

Data Availability

Data will be made available on request.

Acknowledgement

Appendix A. Supporting information

Supplementary data associated with this article can be found in the online version at doi:10.1016/j.apcatb.2023.123091.

References

[1] S.C. Peter, Reduction of CO_2 to chemicals and fuels: a solution to global warming and energy crisis, ACS Energy Lett. 3 (2018) 1557–1561.

[2] M. Shoeb, M. Mobin, M.A. Rauf, S.M. Adnan, M.Y. Ansari, Graphene nickelcopper nanocomposite (Gr@NiCu NCs) as a binder free electrode for high energy density supercapacitor and antimicrobial application, J. Mater. 7 (2021) 815–827.

[3] A.Z. Al Shaqsi, K. Sopian, A. Al-Hinai, Review of energy storage services, applications, limitations, and benefits, Energy Rep. 6 (2020) 288–306.

[4] S.W. Ragsdale, E. Pierce, Acetogenesis and the Wood–Ljungdahl pathway of CO_2 fixation, Biochim. Et Biophys. Acta (BBA) - Proteins Proteom. 1784 (2008) 1873–1898.

[5] K. Rabaey, R.A. Rozendal, Microbial electrosynthesis — revisiting the electrical route for microbial production, Nat. Rev. Microbiol. 8 (2010) 706–716.

[6] E. Blanchet, F. Duquenne, Y. Rafrafi, L. Etcheverry, B. Erable, A. Bergel, Importance of the hydrogen route in up-scaling electrosynthesis for microbial CO_2 reduction, Energy Environ. Sci. 8 (2015) 3731–3744.

[7] A.H. Anwer, N. Khan, M.D. Khan, S. Shakeel, M.Z. Khan, Redox mediators as cathode catalyst to boost the microbial electro-synthesis of biofuel product from carbon dioxide, Fuel 302 (2021), 121124.

[8] T. Zhang, H. Nie, T.S. Bain, H. Lu, M. Cui, O.L. Snoeyenbos-West, A.E. Franks, K. P. Nevin, T.P. Russell, D.R. Lovley, Improved cathode materials for microbial electrosynthesis, Energy Environ. Sci. 6 (2013) 217–224.

[9] H. Nie, T. Zhang, M. Cui, H. Lu, D.R. Lovley, T.P. Russell, Improved cathode for high efficient microbial-catalyzed reduction in microbial electrosynthesis cells, Phys. Chem. Chem. Phys. 15 (2013) 14290–14294.

[10] S. Tian, H. Wang, Z. Dong, Y. Yang, H. Yuan, Q. Huang, T.-s Song, J. Xie, Mo2C-induced hydrogen production enhances microbial electrosynthesis of acetate from CO_2 reduction, Biotechnol. Biofuels 12 (2019) 71.

[11] A.H. Anwer, M.D. Khan, N. Khan, A.S. Nizami, M. Rehan, M.Z. Khan, Development of novel MnO2 coated carbon felt cathode for microbial electroreduction of CO_2 to biofuels, J. Environ. Manag. 249 (2019), 109376.

[12] E.M. Nichols, J.J. Gallagher, C. Liu, Y. Su, J. Resasco, Y. Yu, Y. Sun, P. Yang, M.C.Y. Chang, C.J. Chang, Hybrid bioinorganic approach to solar-to-chemical conversion 112 2015 11461 11466.

[13] K.K. Sakimoto, A.B. Wong, P. Yang, Self-photosensitization of nonphotosynthetic bacteria for solar-to-chemical production, 351 (2016) 74–77.

[14] F. Fischer, Photoelectrode, photovoltaic and photosynthetic microbial fuel cells, Renew. Sustain. Energy Rev. 90 (2018) 16–27.

[15] K. Sasaki, D. Sasaki, K. Kamiya, S. Nakanishi, A. Kondo, S. Kato, Electrochemical biotechnologies minimizing the required electrode assemblies, Curr. Opin. Biotechnol. 50 (2018) 182–188.

[16] C. Liu, J.J. Gallagher, K.K. Sakimoto, E.M. Nichols, C.J. Chang, M.C.Y. Chang, P. Yang, Nanowire–bacteria hybrids for unassisted solar carbon dioxide fixation to value-added chemicals, Nano Lett. 15 (2015) 3634–3639.

[17] M. Shoeb, M. Mobin, S.M. Adnan, I.I. Ansari, M.N. Khan, S. Zaidi, M.Y. Ansari, Facile synthesis of a Gr-Ag/PIn nanocomposite as a binder free electrode for high-performance supercapacitor application, Surf. Interfaces 28 (2022), 101650.

[18] Z. Cai, L. Huang, X. Quan, Z. Zhao, Y. Shi, G. Li Puma, Acetate production from inorganic carbon (HCO3-) in photo-assisted biocathode microbial electrosynthesis systems using WO3/MoO3/g-C3N4 heterojunctions and Serratia marcescens species, Appl. Catal. B: Environ. 267 (2020), 118611.

[19] W. Kong, L. Huang, X. Quan, Z. Zhao, G. Li Puma, Efficient production of acetate from inorganic carbon (HCO3–) in microbial electrosynthesis systems incorporating Ag3PO4/g-C3N4 anaerobic photo-assisted biocathodes, Appl. Catal. B: Environ. 284 (2021), 119696.

[20] S. Bajracharya, S. Srikanth, G. Mohanakrishna, R. Zacharia, D.P. Strik, D. Pant, Biotransformation of carbon dioxide in bioelectrochemical systems: state of the art and future prospects, J. Power Sources 356 (2017) 256–273.

[21] Y. Xiang, G. Liu, R. Zhang, Y. Lu, H. Luo, High-efficient acetate production from carbon dioxide using a bioanode microbial electrosynthesis system with bipolar membrane, Bioresour. Technol. 233 (2017) 227–235.

[22] D. Zanardo, G. Forghieri, S. Tieuli, E. Ghedini, F. Menegazzo, A. Di Michele, G. Cruciani, M. Signoretto, Effects of SiO2-based scaffolds in TiO2 photocatalyzed CO_2 reduction, Catal. Today 387 (2022) 54–60.

[23] L. Wang, H. Zhou, H. Zhang, Y. Song, H. Zhang, X. Qian, SiO2@TiO2 core@shell nanoparticles deposited on 2D-layered ZnIn2S4 to form a ternary heterostructure for simultaneous photocatalytic hydrogen production and organic pollutant degradation, Inorg. Chem. 59 (2020) 2278–2287.

[24] A. Ali, M. Shoeb, B. Li, M.A. Khan, Photocatalytic degradation of antibiotic drug and dye pollutants under visible-light irradiation by reduced graphene oxide decorated MoO3/TiO2 nanocomposite, Mater. Sci. Semicond. Process. 150 (2022), 106974.

[25] M. Shoeb, M. Mobin, A. Ali, S. Zaman, A.H. Naqvi, Graphene-mesoporous anatase TiO2 nanocomposite: A highly efficient and recyclable heterogeneous catalyst for one-pot multicomponent synthesis of benzodiazepine derivatives, 32 (2018) e3961.

[26] Y. Ma, X. Wang, Y. Jia, X. Chen, H. Han, C. Li, Titanium dioxide-based nanomaterials for photocatalytic fuel generations, Chem. Rev. 114 (2014) 9987–10043.

[27] K. Mori, H. Yamashita, M. Anpo, Photocatalytic reduction of CO_2 with H2O on various titanium oxide photocatalysts, RSC Adv. 2 (2012) 3165–3172.

[28] Y. Zhang, Y. Zhao, S. Cao, Z. Yin, L. Cheng, L. Wu, Design and synthesis of hierarchical SiO2@C/TiO2 hollow spheres for high-performance supercapacitors, ACS Appl. Mater. Interfaces 9 (2017) 29982–29991.

[29] S. Yang, Y. Lin, X. Song, P. Zhang, L. Gao, Covalently coupled ultrafine H-TiO2 nanocrystals/nitrogen-doped graphene hybrid materials for high-performance supercapacitor, ACS Appl. Mater. Interfaces 7 (2015) 17884–17892.

[30] X. Sun, M. Xie, G. Wang, H. Sun, A.S. Cavanagh, J.J. Travis, S.M. George, J. Lian, Atomic layer deposition of TiO2 on graphene for supercapacitors, J. Electrochem. Soc. 159 (2012) A364–A369.

[31] L. Lu, Y. Zhu, F. Li, W. Zhuang, K.Y. Chan, X. Lu, Carbon titania mesoporous composite whisker as stable supercapacitor electrode material, J. Mater. Chem. 20 (2010) 7645–7651.

[32] M. Shoeb, B.R. Singh, M. Mobin, G. Afreen, W. Khan, A.H. Naqvi, Kinetic study on mutagenic chemical degradation through three pot synthesiszed graphene@ZnO nanocomposite, PLoS One 10 (2015), e0135055.

[33] M. Shoeb, M. Mobin, M.A. Rauf, M. Owais, A.H. Naqvi, In vitro and in vivo antimicrobial evaluation of graphene–polyindole (Gr@PIn) nanocomposite against methicillin-resistant staphylococcus aureus pathogen, ACS Omega 3 (2018) 9431–9440.

[34] A.H. Anwer, N. Khan, M.F. Umar, M. Rafatullah, M.Z. Khan, Electrodeposited Hybrid Biocathode-Based CO2 Reduction via Microbial Electro-Catalysis to Biofuels, 11 (2021) 223.

[35] L. Huang, Q. Wang, L. Jiang, P. Zhou, X. Quan, B.E. Logan, Adaptively evolving bacterial communities for complete and selective reduction of Cr(VI), Cu(II), and Cd(II) in biocathode bioelectrochemical systems, Environ. Sci. Technol. 49 (2015) 9914–9924.

[36] L. Jourdin, S. Freguia, V. Flexer, J. Keller, Bringing high-rate, CO_2-based microbial electrosynthesis closer to practical implementation through improved electrode design and operating conditions, Environ. Sci. Technol. 50 (2016) 1982–1989.

[37] Q. Wang, L. Huang, X. Quan, G. Li Puma, Sequential anaerobic and electro-Fenton processes mediated by W and Mo oxides for degradation/mineralization of azo dye methyl orange in photo assisted microbial fuel cells, Appl. Catal. B: Environ. 245 (2019) 672–680.

[38] Q. Wang, Z. Cai, L. Huang, Y. Pan, X. Quan, G. Li Puma, Intensified degradation and mineralization of antibiotic metronidazole in photo-assisted microbial fuel cells with Mo-W catalytic cathodes under anaerobic or aerobic conditions in the presence of Fe(III), Chem. Eng. J. 376 (2019), 119566.

[39] Y. Qian, L. Huang, P. Zhou, F. Tian, G.L. Puma, Reduction of Cu(II) and simultaneous production of acetate from inorganic carbon by Serratia Marcescens biofilms and plankton cells in microbial electrosynthesis systems, Sci. Total Environ. 666 (2019) 114–125.

[40] S.H. Joo, A.J. Feitz, D.L. Sedlak, T.D. Waite, Quantification of the oxidizing capacity of nanoparticulate zero-valent iron, Environ. Sci. Technol. 39 (2005) 1263–1268.

[41] I.A. Katsoyiannis, T. Ruettimann, S.J. Hug, pH dependence of fenton reagent generation and As(III) oxidation and removal by corrosion of zero valent iron in aerated water, Environ. Sci. Technol. 42 (2008) 7424–7430.

[42] B. Wang, C. Li, H. Cui, J. Zhang, J. Zhai, Q. Li, Shifting mechanisms in the initial stage of dye photodegradation by hollow TiO2 nanospheres, J. Mater. Sci. 49 (2014) 1336–1344.

[43] S. Jorfi, B. Kakavandi, H.R. Motlagh, M. Ahmadi, N. Jaafarzadeh, A novel combination of oxidative degradation for benzotriazole removal using TiO2 loaded on FeIIFe2IIIO4@C as an efficient activator of peroxymonosulfate, Appl. Catal. B: Environ. 219 (2017) 216–230.

[44] B.E. Conway, Electrochemical Supercapacitors: Scientific Fundamentals and Technological Applications, Springer Science & Business Media, 2013.

[45] M. Lu, Supercapacitors: Materials, Systems, and Applications, John Wiley & Sons, 2013.

[46] A.H. Anwer, M.Z. Ansari, F. Mashkoor, S. Zhu, M. Shoeb, C. Jeong, Synergistic effect of carbon nanotube and Tri-metallic MOF nanoarchitecture for electrochemical high-performance asymmetric supercapacitor applications and their charge storage mechanism, J. Alloy. Compd. (2023) 170038.

[47] A. Ali, M. Shoeb, Y. Li, B. Li, M.A. Khan, Enhanced photocatalytic degradation of antibiotic drug and dye pollutants by graphene-ordered mesoporous silica (SBA 15)/TiO2 nanocomposite under visible-light irradiation, J. Mol. Liq. 324 (2021), 114696.

[48] Y. Hou, Y. Gan, Z. Yu, X. Chen, L. Qian, B. Zhang, L. Huang, J. Huang, Solar promoted azo dye degradation and energy production in the bio-photoelectrochemical system with a g-C3N4/BiOBr heterojunction photocathode, J. Power Sources 371 (2017) 26–34.

[49] Y. He, L. Zhang, X. Wang, Y. Wu, H. Lin, L. Zhao, W. Weng, H. Wan, M. Fan, Enhanced photodegradation activity of methyl orange over Z-scheme type MoO3–g-C3N4 composite under visible light irradiation, RSC Adv. 4 (2014) 13610–13619.

[50] Y. Hou, G. Yuan, S. Wang, Z. Yu, S. Qin, L. Tu, Y. Yan, X. Chen, H. Zhu, Y. Tang, Nitrofurazone degradation in the self-biased bio-photoelectrochemical system: g-C3N4/CdS photocathode characterization, degradation performance, mechanism and pathways, J. Hazard. Mater. 384 (2020), 121438.

[51] L. Jourdin, S. Freguia, B.C. Donose, J. Chen, G.G. Wallace, J. Keller, V. Flexer, A novel carbon nanotube modified scaffold as an efficient biocathode material for improved microbial electrosynthesis, J. Mater. Chem. A 2 (2014) 13093–13102.

[52] L. Jourdin, T. Grieger, J. Monetti, V. Flexer, S. Freguia, Y. Lu, J. Chen, M. Romano, G.G. Wallace, J. Keller, High acetic acid production rate obtained by microbial electrosynthesis from carbon dioxide, Environ. Sci. Technol. 49 (2015) 13566–13574.

[53] S. Bajracharya, K. Vanbroekhoven, C.J.N. Buisman, D.P.B.T.B. Strik, D. Pant, Bioelectrochemical conversion of CO2 to chemicals: CO2 as a next generation feedstock for electricity-driven bioproduction in batch and continuous modes, Faraday Discuss. 202 (2017) 433–449.

[54] T.-s Song, H. Zhang, H. Liu, D. Zhang, H. Wang, Y. Yang, H. Yuan, J. Xie, High efficiency microbial electrosynthesis of acetate from carbon dioxide by a self-assembled electroactive biofilm, Bioresour. Technol. 243 (2017) 573–582.

[55] T.-s Song, K. Fei, H. Zhang, H. Yuan, Y. Yang, P. Ouyang, J. Xie, High efficiency microbial electrosynthesis of acetate from carbon dioxide using a novel graphene–nickel foam as cathode, J. Chem. Technol. Biotechnol. 93 (2018) 457–466.

[56] G. Mohanakrishna, K. Vanbroekhoven, D. Pant, Imperative role of applied potential and inorganic carbon source on acetate production through microbial electrosynthesis, J. CO2 Util. 15 (2016) 57–64.

[57] G. Mohanakrishna, K. Vanbroekhoven, D. Pant, Impact of dissolved carbon dioxide concentration on the process parameters during its conversion to acetate through microbial electrosynthesis, React. Chem. Eng. 3 (2018) 371–378.

[58] Z. Dong, H. Wang, S. Tian, Y. Yang, H. Yuan, Q. Huang, T.-s Song, J. Xie, Fluidized granular activated carbon electrode for efficient microbial electrosynthesis of acetate from carbon dioxide, Bioresour. Technol. 269 (2018) 203–209.

[59] Q.-Y. Chen, J.-S. Liu, Y. Liu, Y.-H. Wang, Hydrogen production on TiO2 nanorod arrays cathode coupling with bio-anode with additional electricity generation, J. Power Sources 238 (2013) 345–349.

[60] K. Yu, X. Hu, K. Yao, P. Luo, X. Wang, H. Wang, Preparation of an ultrathin 2D/2D rGO/g-C3N4 nanocomposite with enhanced visible-light-driven photocatalytic performance, RSC Adv. 7 (2017) 36793–36799.

[61] S. Bajracharya, B. van den Burg, K. Vanbroekhoven, H. De Wever, C.J.N. Buisman, D. Pant, D.P.B.T.B. Strik, In situ acetate separation in microbial electrosynthesis from CO2 using ion-exchange resin, Electrochim. Acta 237 (2017) 267–275.

[62] B.E. Logan, Essential Data and Techniques for Conducting Microbial Fuel Cell and other Types of Bioelectrochemical System Experiments, 5 (2012) 988–994.

[63] B. Kakavandi, E. Dehghanifard, P. Gholami, M. Noorisepehr, B. MirzaHedayat, Photocatalytic activation of peroxydisulfate by magnetic Fe3O4@SiO2@TiO2/rGO core–shell towards degradation and mineralization of metronidazole, Appl. Surf. Sci. 570 (2021) 151145.

[64] A. Ray, A. Roy, M. Ghosh, J. Alberto Ramos-Ramón, S. Saha, U. Pal, S. K. Bhattacharya, S. Das, Study on charge storage mechanism in working electrodes fabricated by sol-gel derived spinel NiMn2O4 nanoparticles for supercapacitor application, Appl. Surf. Sci. 463 (2019) 513–525.

[65] M.Z. Ansari, N. Parveen, D.K. Nandi, R. Ramesh, S.A. Ansari, T. Cheon, S.-H. Kim, Enhanced activity of highly conformal and layered tin sulfide (SnSx) prepared by atomic layer deposition (ALD) on 3D metal scaffold towards high performance supercapacitor electrode, Sci. Rep. 9 (2019) 10225.

[66] M.Z. Ansari, S.A. Ansari, N. Parveen, M.H. Cho, T. Song, Lithium ion storage ability, supercapacitor electrode performance, and photocatalytic performance of tungsten disulfide nanosheets, New J. Chem. 42 (2018) 5859–5867.

[67] J.S. Ko, C.-H. Lai, J.W. Long, D.R. Rolison, B. Dunn, J. Nelson Weker, Differentiating double-layer, psuedocapacitance, and battery-like mechanisms by analyzing impedance measurements in three dimensions, ACS Appl. Mater. Interfaces 12 (2020) 14071–14078.

[68] A. Cymann-Sachajdak, M. Graczyk-Zajac, G. Trykowski, M. Wilamowska-Zawłocka, Understanding the capacitance of thin composite films based on conducting polymer and carbon nanostructures in aqueous electrolytes, Electrochim. Acta 383 (2021), 138356.

[69] A.-Y. Lo, C.-C. Chang, Y.-W. Lai, P.-R. Chen, B.-C. Xu, Improving the supercapacitor performance by dispersing SiO2 microspheres in electrodes, ACS Omega 5 (2020) 11522–11528.

[70] K.C. Leonard, W.E. Suyama, M.A. Anderson, Improvement of electrochemical capacitor electrodes using SiO2 nanoparticles, Electrochim. Acta 56 (2011) 10137–10144.

[71] M. Sajjad, Y. Jiang, L. Guan, X. Chen, A. Iqbal, S. Zhang, Y. Ren, X. Zhou, Z. Liu, NiCo2S4 nanosheet grafted SiO2@C core-shelled spheres as a novel electrode for high performance supercapacitors, Nanotechnology 31 (2020), 045403.

[72] H. Wang, R. Liu, C. Yang, Q. Hao, X. Wang, K. Gong, J. Wu, Y. Hu, Z. Li, J. Jiang, Smart and designable graphene–SiO2 nanocomposites with multifunctional applications in silicone elastomers and polyaniline supercapacitors, RSC Adv. 7 (2017) 11478–11490.

[73] A. Maitra, A.K. Das, R. Bera, S.K. Karan, S. Paria, S.K. Si, B.B. Khatua, An approach to fabricate PDMS encapsulated all-solid-state advanced asymmetric supercapacitor device with vertically aligned hierarchical Zn–Fe–Co ternary oxide nanowire and nitrogen doped graphene nanosheet for high power device applications, ACS Appl. Mater. Interfaces 9 (2017) 5947–5958.

[74] Y. Zhang, H. Chen, S. Wang, W. Shao, W. Qin, X. Zhao, F. Kong, Facile fabrication and structure control of SiO2/carbon via in situ doping from liquefied bio-based sawdust for supercapacitor applications, Ind. Crop. Prod. 151 (2020), 112490.